



HAL
open science

Predicting the Electrical Conductivity of Partially Saturated Frozen Porous Media, a Fractal Model for Wide Ranges of Temperature and Salinity

Haoliang Luo, Damien Jougnot, Anne Jost, Jidong Teng, Aida Mendieta, Gang Lin, Luong Duy Thanh

► **To cite this version:**

Haoliang Luo, Damien Jougnot, Anne Jost, Jidong Teng, Aida Mendieta, et al.. Predicting the Electrical Conductivity of Partially Saturated Frozen Porous Media, a Fractal Model for Wide Ranges of Temperature and Salinity. *Water Resources Research*, 2024, 60 (3), 10.1029/2023wr034845 . hal-04531358

HAL Id: hal-04531358

<https://hal.sorbonne-universite.fr/hal-04531358>

Submitted on 3 Apr 2024

HAL is a multi-disciplinary open access archive for the deposit and dissemination of scientific research documents, whether they are published or not. The documents may come from teaching and research institutions in France or abroad, or from public or private research centers.

L'archive ouverte pluridisciplinaire **HAL**, est destinée au dépôt et à la diffusion de documents scientifiques de niveau recherche, publiés ou non, émanant des établissements d'enseignement et de recherche français ou étrangers, des laboratoires publics ou privés.



Distributed under a Creative Commons Attribution 4.0 International License

Water Resources Research®

RESEARCH ARTICLE

10.1029/2023WR034845

Key Points:

- We propose a new capillary bundle model that accounts for fractal pore size and tortuosity distributions in the electrical conductivity of frozen porous media
- Electrical conductivity changes with decreasing temperature in two stages: a gradual decrease followed by a sharp drop below the freezing temperature
- This new model correctly reproduces experimental data in a wide temperature, water saturation, and salinity ranges

Supporting Information:

Supporting Information may be found in the online version of this article.

Correspondence to:

H. Luo and D. Jougnot,
haoliang.luo@sorbonne-universite.fr;
damien.jougnot@sorbonne-universite.fr

Citation:

Luo, H., Jougnot, D., Jost, A., Teng, J., Mendieta, A., Lin, G., & Thanh, L. D. (2024). Predicting the electrical conductivity of partially saturated frozen porous media, a fractal model for wide ranges of temperature and salinity. *Water Resources Research*, 60, e2023WR034845. <https://doi.org/10.1029/2023WR034845>

Received 7 MAR 2023

Accepted 9 MAR 2024






Author Contributions:

Conceptualization: Haoliang Luo, Damien Jougnot, Anne Jost, Luong Duy Thanh
Data curation: Haoliang Luo, Gang Lin
Formal analysis: Haoliang Luo
Funding acquisition: Damien Jougnot, Anne Jost, Jidong Teng
Investigation: Haoliang Luo
Methodology: Haoliang Luo, Damien Jougnot, Anne Jost, Jidong Teng, Aida Mendieta, Gang Lin, Luong Duy Thanh

© 2024. The Authors.

This is an open access article under the terms of the [Creative Commons Attribution License](https://creativecommons.org/licenses/by/4.0/), which permits use, distribution and reproduction in any medium, provided the original work is properly cited.

Predicting the Electrical Conductivity of Partially Saturated Frozen Porous Media, a Fractal Model for Wide Ranges of Temperature and Salinity

Haoliang Luo¹ , Damien Jougnot¹ , Anne Jost¹ , Jidong Teng² , Aida Mendieta¹ , Gang Lin³, and Luong Duy Thanh⁴

¹Sorbonne Université, CNRS, UMR 7619 METIS, Paris, France, ²School of Civil Engineering, Central South University, Changsha, China, ³Laboratoire de Géologie, Ecole Normale Supérieure, Paris, France, ⁴Thuyloi University, Dong Da, Vietnam

Abstract The quantitative determination of liquid water content and salinity in soils is crucial for the preservation of hydrological environments and engineering infrastructures, especially in frozen regions. Electrical conductivity, as a fundamental physical parameter in electrical and electromagnetic non-destructive techniques, varies significantly with the physical and chemical properties, such as pore water conductivity, salinity, water saturation, and temperature. In this study, accounting for pore size and tortuous length following fractal distributions, we develop a new capillary bundle model for variation of electrical conductivity as a function of temperature in broad water saturation and salinity ranges. In this new model, we consider the contributions of bulk and surface conductivities to the total electrical conductivity. To test this model, a series of laboratory experiments were carried out for different initial water saturations and salinities using an electrical resistance apparatus and a nuclear magnetic resonance method. The experimental results show that unfrozen water saturation and ionic concentration affect the electrical conductivity of unsaturated frozen soils. Furthermore, the proposed model is capable of fitting the main trends of the experimental data from the literature and acquired in this study in unfrozen-frozen conditions for different water contents. Relying on the proposed model, we also determine the expression of the apparent formation factor, which is significantly sensitive to porosity, water saturation, and temperature. The predicted values of the apparent formation factor also agree very well with the experimental data. This new capillary bundle model provides a new perspective in interpreting electrical monitoring to easily deduce changes in key variables in the cryosphere such as liquid water content and moisture gradients.

1. Introduction

Frozen water is the main fresh water storage system from five types of storages defined by Gleeson et al. (2020). It plays a major role in the global water cycle and is by definition highly sensitive to climate change (Intergovernmental Panel on Climate Change, 2019). Moreover, in frozen zones, the freezing and melting processes affect the hydrological environment (Christensen et al., 2013; Hayashi et al., 2003; He et al., 2016; Oquist et al., 2009; Watanabe & Osada, 2017) and engineering infrastructure developments (Tai et al., 2018, 2020; Teng et al., 2019, 2022; Wen et al., 2012). On the one hand, the degradation of frozen soils results in microbial activities, the growth of thermokarst lakes, and biogeochemical processes (Loisel et al., 2021; Oquist et al., 2009; Watanabe & Osada, 2017). On the other hand, engineering constructions on frozen soils are also affected by the presence of frozen layers, leading to frost-heave and thaw-weakening damages, which particularly affect the safety performance of high-speed railways due to the strict deformation requirement of subgrade foundations (Bai et al., 2018; Christensen et al., 2013; Hayashi et al., 2003; Teng et al., 2019, 2022; Y. Z. Zhang et al., 2019). Therefore, it is essential to have a good understanding of the physical properties of frozen layers in order to study and monitor thermo-hydro-mechanical processes of frozen soils. For example, it is important to study how the temporal and spatial evolutions of the liquid water saturation and salinity contribute to the hydromechanical properties and their role in moisture transfer and potential ice formation.

Liquid water still exists in soil pores when temperature falls below the freezing temperature due to soil water potential (including the soil grain matrix potential and chemical potential) (Andersland & Ladanyi, 2004; Hu et al., 2023; Jin et al., 2020; C. Zhang & Liu, 2018; C. Zhang & Lu, 2018; Zhou et al., 2020). The relationship between liquid water content and temperature is described by the soil freezing characteristic curve (SFCC). The

Project administration: Damien Jougnot, Anne Jost, Jidong Teng

Resources: Damien Jougnot

Software: Haoliang Luo, Damien Jougnot, Aida Mendieta

Supervision: Damien Jougnot, Anne Jost, Jidong Teng

Validation: Haoliang Luo

Visualization: Damien Jougnot, Anne Jost, Aida Mendieta, Luong Duy Thanh

Writing – original draft: Haoliang Luo

Writing – review & editing: Damien Jougnot, Anne Jost, Jidong Teng, Aida Mendieta, Gang Lin, Luong Duy Thanh

type of soluble salts and the salinity affect the variation of the unfrozen water content of the frozen porous medium (Banin & Anderson, 1974; Watanabe & Mizoguchi, 2002; Xiao et al., 2018). For an ideal dilute solution (e.g., containing NaCl), as the experimental temperature decreases, liquid water in the pore is converted to bulk ice. As the liquid water content diminishes below freezing temperature, the salts are discharged from the solid ice into the pore water, thus the ionic concentration of the liquid water increases when temperature declines, leading to the freezing temperature of the remaining liquid water in frozen soils that is further depressed (L. Y. Wang et al., 2021; Zhou et al., 2020). The initial saturation condition (i.e., the equivalent water saturation above freezing conditions) is also another considerable factor affecting the hydromechanical issues. Variations in initial saturation are susceptible to cause frost heave in engineering structures. Bai et al. (2018) and Niu et al. (2017) discovered significant frost heave in the subgrade foundation of high-speed railway using TDR-3 soil moisture sensors and displacement sensors through long-term field monitoring (e.g., Harbin-Dalian high-speed railway subgrade). They attributed the ice accumulation in the railway subgrades to air transfer in unsaturated frozen soils. Teng et al. (2020) directly measured the liquid water content and corresponding soil temperature for different initial water saturations using the nuclear magnetic resonance (NMR) method and investigated the evolution of the liquid water saturation with temperature. Amankwah et al. (2021) designed laboratory and field experiments on the unfrozen water content with different types of frozen soils, initial water saturations, and salinities using HydraProbes® sensors. They then compared the dependence of the liquid water content on the salt exclusion and initial water saturation effects. Consequently, for both experimental and theoretical aspects, accurate determinations of unfrozen water content and ionic concentration at freezing temperature over a wide range of temperature, water saturation and salinity are the basis for understanding and addressing the thermo-hydro-mechanical issues in cold regions.

The selection of appropriate experimental methods for subsurface characterization is of crucial importance. For this goal, the field of geophysics can provide a wide category of techniques that now constitute the well-established field of hydrogeophysics (e.g., Binley et al., 2015; Hermans et al., 2023). Electrical and electromagnetic methods, including electrical resistivity tomography, self-potential (SP), and (spectral) induced polarization (SIP), can be used to investigate the water distribution and solute concentration of porous media at various scales, from small-scale (e.g., from micrometer to several meters) laboratory measurements to long-term (e.g., over several months) large-scale (e.g., from several meters to several kilometers) field monitoring. In terms of laboratory-scale measurements, as a typical non-destructive measurement technique, the electrical and electromagnetic methods have been adopted to measure the evolution of water saturation, hydraulic conductivity, and salinity in recent years. For instance, using IP techniques, Revil, Coperey, Deng, et al. (2018) and Revil et al. (2017) investigated the complex conductivity of soil samples to determine the relationship of the complex conductivity (real and imaginary parts) with frequency for varying water saturations and salinities above the freezing temperature. In terms of long-term large-scale monitoring, the electrical and electromagnetic methods can be used as a fluid tracker to non-destructively monitor the distribution and dynamics of the liquid water in shallow aquifers, the salinity of and transport of subsurface pollutants (e.g., Revil et al., 2012), such that they can be applied in the field monitoring of the subsurface, from fully saturated conditions (e.g., Kemna et al., 2002; Pollock & Cirpka, 2012) to partially saturated conditions (Binley et al., 2002; Haarder et al., 2015; Jougnot et al., 2015). These geoelectrical methods are increasingly applied in cold regions, where they are used to remotely monitor the dynamics of the active layer thickness in the permafrost (Bussière et al., 2022; Duvillard et al., 2018; Pedrazas et al., 2020), the unsaturated flow in melting snow (Clayton, 2017, 2021; Kulesa et al., 2003, 2012), snowmelt infiltration, and the spatial and temporal distribution of unfrozen and frozen zones (Coperey, Revil, Abdulsamad, et al., 2019; Coperey, Revil, & Stutz, 2019; Duvillard et al., 2018, 2021; Hauck et al., 2011). These geophysical methods appear to be an appropriate way to meet the needs of measurements in permafrost environments, particularly for distinguishing between unfrozen and frozen areas, due to the sensitivity of geophysical properties to the contrast between liquid and solid water. For example, the electrical conductivity of frozen layers varies by several orders of magnitude when compared to a porous medium above freezing temperature. In particular, some studies explored the relationship between electrical conductivity and temperature at freezing temperature for different soil samples using laboratory geophysical methods, and evaluated the unfrozen water and ice contents (Holloway & Lewkowicz, 2019; Lai et al., 2021; Luo et al., 2021, 2023; Oldenborger & LeBlanc, 2018). However, there are few laboratory studies on the effects of initial water saturation and salinity on the electrical conductivity of partially saturated frozen soils below freezing temperature.

From a theoretical development point of view, it is crucial to relate the electrical conductivity not only to pore fluid properties such as water saturation, ionic concentration, and porosity, but also to mineral surface properties such as Cationic Exchange Capacity (CEC) or Specific Surface Area. Several physically-based models have been proposed to relate the electrical conductivity to temperature in frost state. As reported in the literature, they can be divided into (a) empirical relationships between the electrical conductivity and temperature (e.g., Dafflon et al., 2016; Herring et al., 2019), (b) mathematical models in relation to the electrical theory (e.g., Shan et al., 2015; Tang et al., 2018), and (c) capillary bundle models (e.g., Coperey, Revil, Abdulsamad, et al., 2019; Luo et al., 2023; Ming et al., 2020). In particular, Luo et al. (2023) formally developed a physically-based model using the Gibbs-Thomson expression (unfrozen water saturation) and the surface complexation model considering the effect of surface conduction for fully saturated conditions. However, the above electrical conductivity models do not account for the effects of different initial water saturations and salinities, and do not explicit the contributions of bulk conduction from liquid water, surface conduction from mineral-water, bulk ice-water and air-water interface to the total electrical conductivity. To summarize, there are few experiments or physically-based models that describe the relationship between electrical conductivity and temperature while taking into account the effects of different initial water saturations and salinities.

In this work, we consider distributions of capillary radii and tortuous lengths obeying fractal distributions. The total conductance of the three types of capillaries (occupied by air, bulk ice, and capillary water) is determined by Gibbs-Thomson and Young-Laplace effects as well as by the surface complexation model. Besides, a new capillary bundle model for partially saturated conditions is proposed by using an upscaling procedure, which considers the effects of bulk and surface conductions. Based primarily on an electrical resistance apparatus and the NMR method, a series of laboratory experiments were carried out to study the influences of initial water saturation and salinity on electrical conductivity under unfrozen and frozen conditions. Furthermore, based on the proposed physically-based model in this study, we analyze the dependence of the model parameters on the electrical conductivity in frozen porous media. Additionally, the proposed model is verified with literature data and new experimental data from this study. Finally, we utilize the proposed model to determine apparent formation factors (i.e., the ratio between the water conductivity and the medium conductivity) that reflect the geometry of the pore space as a function of porosity, water saturation, and temperature.

2. Fractal Theory for Porous Media

The physically-based model builds on the recent electrical conductivity model developed by Luo et al. (2023) to consider an initially unsaturated unfrozen porous medium and various initial salinities. Due to its rotational symmetry and alignment with natural geometry, we assume a cylinder with cross-section area A_{REV} (in m^2) and length L_0 (in m) as a representative elementary volume (REV) of the frozen porous medium, relying on simplification and practical considerations in modeling and analysis. It is composed of an equivalent bundle of capillary tubes (oriented along the length of the REV) following a fractal pore size distribution (PSD), and the radii size varies from minimum radius r_{min} (in m) to maximum radius r_{max} (in m) (Figure 1). It is assumed that the fractal distribution governs the cumulative size distribution of pores with radius greater than or equal to r (in, m) (e.g., Tyler & Wheatcraft, 1990; Yu & Cheng, 2002):

$$N(\geq r) = \left(\frac{r_{\text{max}}}{r}\right)^{D_f}, \quad (1)$$

where D_f is the fractal dimension of pore size, and the $N(\geq r)$ represents the number of capillary tubes with radius greater than or equal to r . Fractal distributions can be successfully used to represent porous medium for a variety of Euclidean dimensions (e.g., 3 dimensions for a volume object, 2 dimensions for a surface object and 1 dimension for a line object). Here, we consider that the electrical current flows in the cylindrical REV as a fractal distribution of capillary sections on a plane (i.e., in 2 dimensions), thus the fractal distribution D_f ranges from 1 to 2. Capillary bundle models with this type of fractal PSD have been increasingly used to compute macroscopic geophysical properties (e.g., electrical conductivity as well as charge excess per unit pore volume) and properties related to fluid flow (e.g., porosity, salinity and permeability) in different materials (e.g., Guarracino et al., 2014; Guarracino & Jougnot, 2018; Thanh et al., 2020; Yu et al., 2003).

Therefore, the fractal PSD (the number of pores whose radii are in the infinitesimal range from r to $r + dr$) is given by

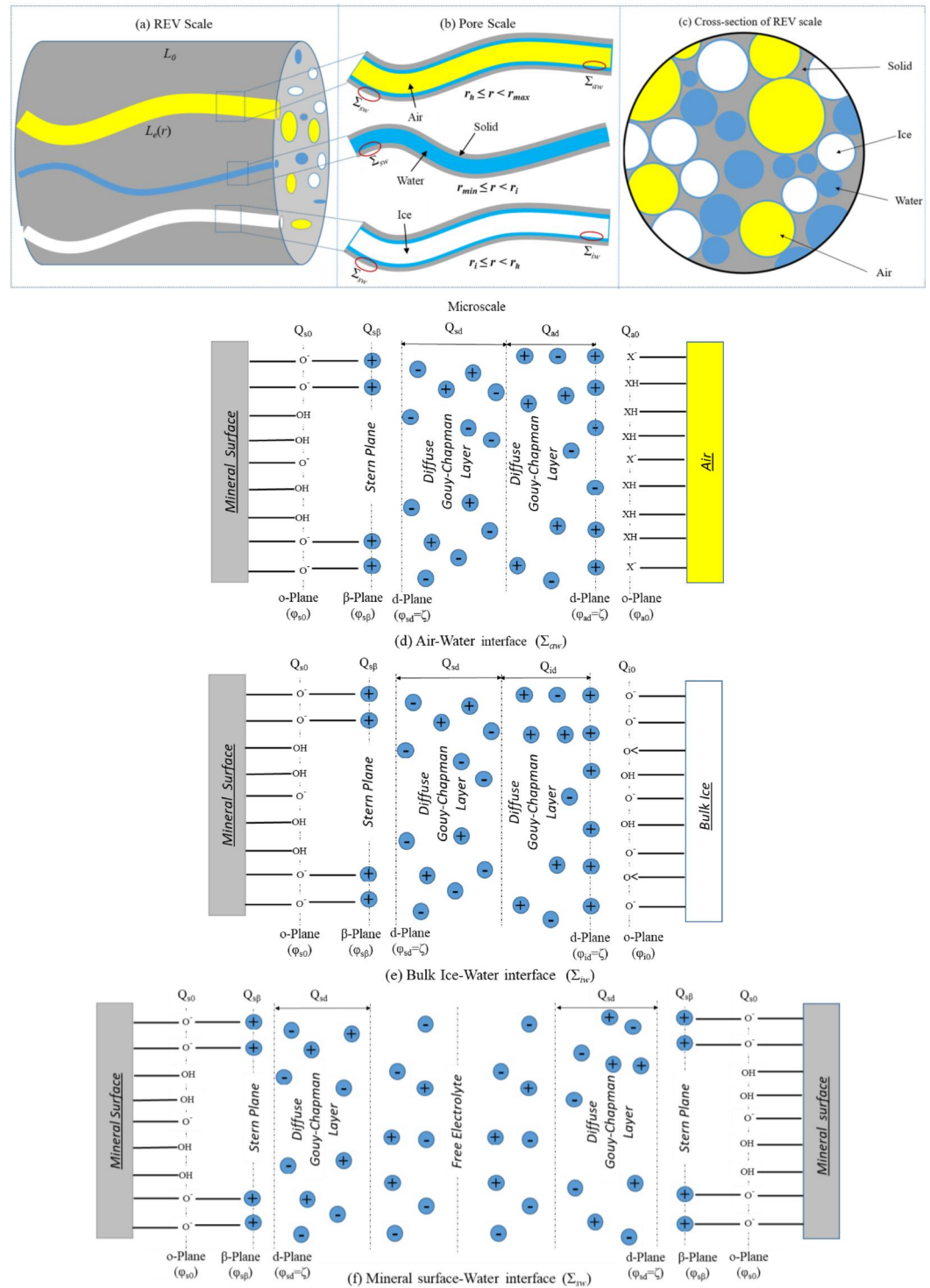


Figure 1. (a) The conceptual electrical model is composed of a large quantity of capillaries in the cylindrical representative elementary volume (REV) scale and the number of capillary tubes follows a fractal pore size distribution (D_p). All the capillaries have a different tortuous length $L_c(r)$ (m) following a fractal distribution (D_e). (b) Based primarily on the Young-Laplace equation and Gibbs-Thomson effect, the capillary is occupied by liquid water, by ice-water film or air-water film depending on its radius (pore scale) at a given temperature and a given initial capillary pressure. (c) The cross-section in the cylindrical REV scale, consisting of mineral solid, liquid water, bulk ice, and air phases. The specific surface conductance is determined by the surface complexation model at the (d) air-water interface, (e) bulk ice-water interface and (f) mineral surface-water interface. The parameters of Q and φ represent the surface charge density and electrical potential, respectively.

$$f(r) = D_f r_{\max}^{D_f} r^{-D_f-1}. \quad (2)$$

The tortuous length L_e (in m) of the pore along the axis of the cylindrical REV is greater than the representative length L_0 (in m) which is the length of the REV (Figure 1). Yu and Cheng (2002) defined a fractal tortuosity that is related to the pore radius by

$$L_e(r) = r^{1-D_e} L_0^{D_e}, \quad (3)$$

where D_e is the fractal dimension (in two dimensions) of the capillary tortuosity with $1 \leq D_e \leq 2$.

In order to obtain the initial capillary radius r_h (in m) filled with liquid water of the unsaturated frozen porous medium, we consider that the REV is drained from an initially fully saturated medium at a pressure head h_m (m), which is determined by the water retention function. For a capillary tube, we use the Young-Laplace equation (Jurin, 1718) to link the pore radius r_h (in m) with the pressure head h_m (m):

$$h_m = \frac{2T_s \cos \beta}{\rho_w g r_h}, \quad (4)$$

where T_s (in N m^{-1}) is surface tension from capillary liquid water, β is the contact angle at liquid water-air interface, g (in m s^{-2}) and ρ_w (in kg m^{-3}) represent acceleration of gravity and bulk water density, respectively. When the radius r (in m) is larger than r_h (in m) determined by Equation 4, the capillary is occupied by air and a thin water film. Therefore, the capillaries whose pore radius ranges from r_{\min} to r_h will remain fully saturated with liquid water.

When the temperature is lowered below the freezing temperature of soils T_m (in K), the pore space can be represented by a bundle of aligned capillary tubes with varying capillary radii, which are filled with either water, or ice-liquid water film. The onset of freezing in the capillary tubes is dictated by the Gibbs-Thomson effect, which relates the freezing temperature of crystals to the curvature of the limiting surface. When the capillary radius is between the initial capillary radius (r_h) and critical capillary radius (r_i), ice is assumed to grow radially from the center of the capillary tube, and the liquid water exists as a thin water film bounded by the solid particle and pore ice phases (e.g., Anderson, 1967). The critical capillary radius r_i can be determined by the Gibbs-Thomson equation ignoring solute effect:

$$r_i = \frac{2\sigma_{sl}}{L_f \rho_i} \frac{T_0}{T_0 - T}, \quad (5)$$

where σ_{sl} denotes the free energy coefficient of the bulk ice-water interface, $\sigma_{sl} = 0.029 \text{ J/m}^2$; L_f is the latent heat of phase transformation, $L_f = 3.35 \times 10^5 \text{ J/kg}$; ρ_i represents the bulk ice density, $\rho_i = 917 \text{ kg/m}^3$; T_0 is the freezing temperature of pure liquid water (273.15 K), and T is the temperature of pore water in specimens (K).

The electrical conductivity of the partially saturated frozen porous medium is composed of the bulk and surface electrical conductivities in all capillaries (Figure 1). Surface conductivity refers to the excess of electrical conductivity within the electrical double layer (EDL) compared to in the bulk pore water and is integrated over the EDL thickness (Revil & Glover, 1997). Consequently, the following assumptions were made based on the Gibbs-Thomson effect (water freezing) and the Young-Laplace equation (water retention) in this study: (a) for $r_{\min} \leq r < r_i$, liquid water occupies the capillaries and there are both the surface and bulk electrical conductivities at the interface between mineral and liquid water (specific surface conductance Σ_{sw}) (Lebeau & Konrad, 2010; Leroy et al., 2008; Thanh et al., 2019); (b) for $r_i \leq r < r_h$, capillaries are filled with bulk ice and there are the surface conductivities between the mineral-liquid water and the bulk ice-liquid water interfaces (specific surface conductances Σ_{sw} and Σ_{iw}) (Daigle, 2021; Lebeau & Konrad, 2012; Luo et al., 2023; Watanabe & Flury, 2008); (c) for $r_h \leq r < r_{\max}$, capillaries are occupied by air and a thin water film and there are the surface electrical conductivities from the mineral-liquid water and the air-liquid water interfaces (specific surface conductances Σ_{sw} and Σ_{aw}) (Leroy et al., 2012; Thanh et al., 2020). In addition, we exclude the capillaries tubes of completely air-filled and completely ice-filled pores, that is, no water film.

The following conceptual technique was applied to calculate the electrical conductivity of the unsaturated frozen porous materials: in accordance with the surface complexation model, we can first derive the electrical conductance at the pore scale, which is regarded as the sum of the three types of capillary (mainly filled with either liquid water, bulk ice, or air), then the physically-based model is determined by an upscaling procedure that describes the evolution of the electrical conductivity at the REV scale.

3. Theoretical Derivation of a Novel Electrical Conductivity Model

3.1. Pore Scale

We consider a capillary tube, which is filled with liquid water, with radius r_1 and length L_e , with $r_{\min} \leq r_1 < r_i$, then the resistance (R_1 in Ω) of the capillary is given by:

$$\frac{1}{R_1} = \frac{\pi r_1^2 \sigma_w}{L_e} + \frac{2\pi r_1 \Sigma_{sw}}{L_e}, \quad (6)$$

where σ_w (in S/m) represents the pore water conductivity and Σ_{sw} (in S) represents the specific surface conductance at the interface between liquid water and the mineral surface.

Then, we consider a capillary tube with radius r_2 and length L_e that is occupied by ice and a thin water film. For $r_i \leq r_2 < r_h$, the resistance (R_2 in Ω) includes the surface conductivity in the mineral-water and bulk ice-water interfaces and is obtained as follows:

$$\frac{1}{R_2} = \frac{2\pi r_2 \Sigma_{sw}}{L_e} + \frac{2\pi r_2 \Sigma_{iw}}{L_e}, \quad (7)$$

where Σ_{iw} (in S) is the specific surface conductance in the bulk ice-water interface.

And we consider a capillary tube (of capillary radius r_3 and length L_e) that is occupied by air ($r_h \leq r_3 < r_{\max}$), then the resistance (R_3 in Ω) of the capillary is given by

$$\frac{1}{R_3} = \frac{2\pi r_3 \Sigma_{sw}}{L_e} + \frac{2\pi r_3 \Sigma_{aw}}{L_e}, \quad (8)$$

where Σ_{aw} (in S) is the specific surface conductance in the air-water interface.

If these three capillaries are placed in parallel, the total conductance $\Sigma(r_1, r_2, r_3)$ (in S) of the three capillaries is given by

$$\Sigma(r_1, r_2, r_3) = \frac{1}{R(r)} = \frac{1}{R_1} + \frac{1}{R_2} + \frac{1}{R_3} = \frac{\pi r_1^2 \sigma_w}{L_e} + \frac{2\pi(r_1 + r_2 + r_3)\Sigma_{sw}}{L_e} + \frac{2\pi r_2 \Sigma_{iw}}{L_e} + \frac{2\pi r_3 \Sigma_{aw}}{L_e}. \quad (9)$$

From Equation 9, we observe that the first term of the expression is the contribution from the pore water conductivity while the second, third and final terms are the contributions from the specific surface conductance of mineral-water, bulk ice-water and air-water interfaces. The pore water conductivity is established as a function of ionic concentration and temperature. The electrochemical properties of mineral, ice and air with thin water film interfaces are estimated by using a surface complexation model, such as the surface charge density and electrical potential. Then, we can determine the specific surface conductance of mineral-water, bulk ice-water, and air-water interfaces using Equations A8, B6, and C6 (Appendix materials). Note that we are treating the conductivity and conduction terms as fixed model quantities involving a large number of parameters, that is, neglecting the effect of the surface site density for varying mineral surfaces.

From these values of the electrolyte concentration, we can compute the relationship between the pore water conductivity (not affected by EDL) and temperature as follows (Luo et al., 2023; Oldenborger, 2021):

$$\sigma_w = \sum_i^n N_A q_i \rho_i^{\text{ref}} C_i^f [1 + \alpha_T (T - T_{\text{ref}})], \quad (10)$$

where N_A represents the Avogadro's number ($6.02 \times 10^{23} \text{ mol}^{-1}$), q_i (in C), C_i^f (in mol/L) are the charge, salinity of species i in the free electrolyte, respectively. β_i^{ref} refers to the reference mobility of ionic species i in the free electrolyte at reference temperature T_{ref} (298 K), and its values are listed in Table S1 in Supporting Information S1, α_T represents the temperature sensitivity factor and in the range 0.019–0.023/K (e.g., Coperey, Revil, Abdulsamad, et al., 2019; Coperey, Revil, & Stutz, 2019).

3.2. REV Scale

In order to determine the electrical conductivity of the partially saturated frozen porous medium, we consider a REV of cross-section area A_{REV} (in m^2) and length L_0 (in m) with a fractal PSD (Equation 2). The electrical resistance R_0 (in Ω) at the partially-saturated REV-scale can be computed as:

$$\frac{1}{R_0} = \int_{r_{\min}}^{r_{\max}} \frac{1}{R(r)} f(r) dr. \quad (11)$$

Consequently, combining Equations 2, 3, 9, and 11, we obtain the following expression for the total resistance at the REV scale:

$$\begin{aligned} \frac{1}{R_0} &= \int_{r_{\min}}^{r_i} \frac{\pi r^2 \sigma_w}{r^{1-D_e} L_0^{D_e}} D_f r_{\max}^{D_f} r^{-D_f-1} dr + \int_{r_{\min}}^{r_{\max}} \frac{2\pi r \Sigma_{sw}}{r^{1-D_e} L_0^{D_e}} D_f r_{\max}^{D_f} r^{-D_f-1} dr \\ &+ \int_{r_i}^{r_h} \frac{2\pi r \Sigma_{iw}}{r^{1-D_e} L_0^{D_e}} D_f r_{\max}^{D_f} r^{-D_f-1} dr + \int_{r_h}^{r_{\max}} \frac{2\pi r \Sigma_{aw}}{r^{1-D_e} L_0^{D_e}} D_f r_{\max}^{D_f} r^{-D_f-1} dr \\ &= \frac{\pi D_f r_{\max}^{D_f}}{L_0^{D_e}} \frac{[r_i^{D_e-D_f+1} - r_{\min}^{D_e-D_f+1}]}{D_e - D_f + 1} \sigma_w + \frac{2\pi D_f r_{\max}^{D_f}}{L_0^{D_e}} \frac{[r_{\max}^{D_e-D_f} - r_{\min}^{D_e-D_f}]}{D_e - D_f} \Sigma_{sw} \\ &+ \frac{2\pi D_f r_{\max}^{D_f}}{L_0^{D_e}} \frac{[r_h^{D_e-D_f} - r_i^{D_e-D_f}]}{D_e - D_f} \Sigma_{iw} + \frac{2\pi D_f r_{\max}^{D_f}}{L_0^{D_e}} \frac{[r_{\max}^{D_e-D_f} - r_h^{D_e-D_f}]}{D_e - D_f} \Sigma_{aw}. \end{aligned} \quad (12)$$

The porosity of the REV can be computed from its definition as the quotient between the volume of pores and the volume of the REV which yields:

$$\phi = \frac{\int_{r_{\min}}^{r_{\max}} \pi r^2 L_e(r) f(r) dr}{A_{\text{REV}} L_0} = \frac{\int_{r_{\min}}^{r_{\max}} \pi r^2 r^{1-D_e} L_0^{D_e} D_f r_{\max}^{D_f} r^{-D_f-1} dr}{A_{\text{REV}} L_0} = \frac{\pi D_f L_0^{D_e-1} r_{\max}^{D_f}}{A_{\text{REV}}} \frac{[r_{\max}^{3-D_e-D_f} - r_{\min}^{3-D_e-D_f}]}{3 - D_e - D_f}. \quad (13)$$

Therefore, the cross-section area of the REV is calculated as

$$A_{\text{REV}} = \frac{\pi D_f L_0^{D_e-1} r_{\max}^{D_f}}{\phi} \frac{[r_{\max}^{3-D_e-D_f} - r_{\min}^{3-D_e-D_f}]}{3 - D_e - D_f}. \quad (14)$$

Additionally, the electrical conductivity of the REV is linked to the resistance of the porous media as

$$\sigma = \frac{L_0}{R_0 A_{\text{REV}}}. \quad (15)$$

From Equations 12–15, the following equation for the electrical conductivity is hereby calculated as:

$$\sigma = \frac{\phi(3 - D_e - D_f)}{L_0^{2D_e-2} (D_e - D_f + 1)} \frac{[r_i^{D_e-D_f+1} - r_{\min}^{D_e-D_f+1}]}{[r_{\max}^{3-D_e-D_f} - r_{\min}^{3-D_e-D_f}]} \sigma_w + \frac{2\phi(3 - D_e - D_f)}{L_0^{2D_e-2} (D_e - D_f)} \frac{[r_{\max}^{D_e-D_f} - r_{\min}^{D_e-D_f}]}{[r_{\max}^{3-D_e-D_f} - r_{\min}^{3-D_e-D_f}]} \Sigma_{sw}$$

$$+ \frac{2\phi(3 - D_e - D_f)}{L_0^{2D_e-2}(D_e - D_f)} \frac{[r_h^{D_e-D_f} - r_i^{D_e-D_f}]}{[r_{\max}^{3-D_e-D_f} - r_{\min}^{3-D_e-D_f}]} \Sigma_{iw} + \frac{2\phi(3 - D_e - D_f)}{L_0^{2D_e-2}(D_e - D_f)} \frac{[r_{\max}^{D_e-D_f} - r_h^{D_e-D_f}]}{[r_{\max}^{3-D_e-D_f} - r_{\min}^{3-D_e-D_f}]} \Sigma_{aw}. \quad (16)$$

We define the effective geometrical tortuosity τ_g^{eff} of the porous medium (Thanh et al., 2019):

$$\tau_g^{\text{eff}} = \left(\frac{L_0}{r_{\max}} \right)^{D_e-1}. \quad (17)$$

From Equation 17, we note that the effective geometrical tortuosity is linked with the fractal dimension for capillary tortuosity (D_e), because the tortuosity length of the pores is assumed to be associated with the capillary radius, that is, smaller capillaries are more tortuous than larger capillaries.

According to Thanh et al. (2019, 2020), τ_g^{eff} can be approximately determined by the basic properties of porous material as

$$\tau_g^{\text{eff}} = \left[\frac{1 - \alpha^{3-D_e-D_f}}{\phi} \frac{\pi D_f}{3 - D_e - D_f} \right]^{\frac{D_e-1}{3-D_e}}, \quad (18)$$

where α represents the ratio of the minimum pore radius to the maximum pore radius, $\alpha = r_{\min}/r_{\max}$.

The initial water saturation ($S_{w,0}$) and the unfrozen water saturation (S_u) can be determined in relation to the critical radius (r_h and r_i , respectively) (detailed derivations can be found in Text S1 in Supporting Information S1), then the electrical conductivity at the REV scale is computed:

$$\begin{aligned} \sigma = & \frac{\phi(3 - D_e - D_f)}{(\tau_g^{\text{eff}})^2 (D_e - D_f + 1)} \frac{\left\{ [\alpha^{3-D_e-D_f} + S_u(1 - \alpha^{3-D_e-D_f})]^{\frac{D_e-D_f+1}{3-D_e-D_f}} - \alpha^{D_e-D_f+1} \right\}}{[1 - \alpha^{3-D_e-D_f}]} \sigma_w \\ & + \frac{2}{r_{\max}} \frac{\phi(3 - D_e - D_f)}{(\tau_g^{\text{eff}})^2 (D_e - D_f)} \frac{[1 - \alpha^{D_e-D_f}]}{[1 - \alpha^{3-D_e-D_f}]} \Sigma_{sw} \\ & + \frac{2}{r_{\max}} \frac{\phi(3 - D_e - D_f)}{(\tau_g^{\text{eff}})^2 (D_e - D_f)} \frac{\left\{ [\alpha^{3-D_e-D_f} + S_{w,0}(1 - \alpha^{3-D_e-D_f})]^{\frac{D_e-D_f}{3-D_e-D_f}} - [\alpha^{3-D_e-D_f} + S_u(1 - \alpha^{3-D_e-D_f})]^{\frac{D_e-D_f}{3-D_e-D_f}} \right\}}{[1 - \alpha^{3-D_e-D_f}]} \Sigma_{iw} \\ & + \frac{2}{r_{\max}} \frac{\phi(3 - D_e - D_f)}{(\tau_g^{\text{eff}})^2 (D_e - D_f)} \frac{\left\{ 1 - [\alpha^{3-D_e-D_f} + S_{w,0}(1 - \alpha^{3-D_e-D_f})]^{\frac{D_e-D_f}{3-D_e-D_f}} \right\}}{[1 - \alpha^{3-D_e-D_f}]} \Sigma_{aw}. \quad (19) \end{aligned}$$

Equation 19 is the proposed model of the electrical conductivity in partially saturated frozen porous media. The first term in Equation 19 is the contribution from the bulk conductivity, and it is sensitive to the pore water conductivity (σ_w), the unfrozen water saturation (S_u), and the microstructural parameters (D_e , D_f , ϕ , α). The second term is the contribution of the surface conductivity of the mineral surface-water interface, and it is linked with the specific surface conductance (Σ_{sw}) and the microstructural parameters (D_e , D_f , r_{\max} , α , ϕ). However, it is independent from the unfrozen water saturation or initial water saturation. Finally, the third and the fourth terms describe the influence of surface conductivity of the bulk ice-water and air-water interfaces, respectively. They are related to the unfrozen water saturation and initial water saturation.

When the temperature of the porous media is below the freezing temperature, the capillary liquid water changes into bulk ice, thus the surface conduction of the bulk ice-water interlayer depends on the liquid water content (S_u and $S_{w,0}$). It should be noted that for $S_u = S_{w,0}$ above the freezing temperature the specific surface conductance in the bulk ice-water interface $\Sigma_{iw} = 0$, and Equation 19 can be simplified to

$$\begin{aligned} \sigma = & \frac{\phi(3 - D_e - D_f)}{\left(\tau_g^{\text{eff}}\right)^2 (D_e - D_f + 1)} \frac{\left\{ \left[\alpha^{3-D_e-D_f} + S_{w,0} (1 - \alpha^{3-D_e-D_f}) \right]^{\frac{D_e-D_f+1}{3-D_e-D_f}} - \alpha^{D_e-D_f+1} \right\}}{\left[1 - \alpha^{3-D_e-D_f} \right]} \sigma_w \\ & + \frac{2}{r_{\max}} \frac{\phi(3 - D_e - D_f)}{\left(\tau_g^{\text{eff}}\right)^2 (D_e - D_f)} \frac{\left[1 - \alpha^{D_e-D_f} \right]}{\left[1 - \alpha^{3-D_e-D_f} \right]} \Sigma_{sw} \\ & + \frac{2}{r_{\max}} \frac{\phi(3 - D_e - D_f)}{\left(\tau_g^{\text{eff}}\right)^2 (D_e - D_f)} \frac{\left\{ 1 - \left[\alpha^{3-D_e-D_f} + S_{w,0} (1 - \alpha^{3-D_e-D_f}) \right]^{\frac{D_e-D_f}{3-D_e-D_f}} \right\}}{\left[1 - \alpha^{3-D_e-D_f} \right]} \Sigma_{aw}. \end{aligned} \quad (20)$$

Equation 20 is the theoretical model for partially saturated conditions above the freezing temperature. It is the same as the theoretical model proposed by Thanh et al. (2020), if we neglect the effect of specific surface conductance from the air-water interface. However, the adsorbed water at air-filled capillary tubes exists as a thin water film and has a remarkable effect on electrical conductivity (Nishiyama & Yokoyama, 2021; Tokunaga, 2011), thus we consider the effect of the surface conductivity at the air-water interface in this study.

It can be observed that for the initial full saturation $S_{w,0} = 1$ (i.e., the specific surface conductance in the air-water interface $\Sigma_{aw} = 0$), and Equation 19 can be simplified to

$$\begin{aligned} \sigma = & \frac{\phi(3 - D_e - D_f)}{\left(\tau_g^{\text{eff}}\right)^2 (D_e - D_f + 1)} \frac{\left\{ \left[\alpha^{3-D_e-D_f} + S_u (1 - \alpha^{3-D_e-D_f}) \right]^{\frac{D_e-D_f+1}{3-D_e-D_f}} - \alpha^{D_e-D_f+1} \right\}}{\left[1 - \alpha^{3-D_e-D_f} \right]} \sigma_w \\ & + \frac{2}{r_{\max}} \frac{\phi(3 - D_e - D_f)}{\left(\tau_g^{\text{eff}}\right)^2 (D_e - D_f)} \frac{\left[1 - \alpha^{D_e-D_f} \right]}{\left[1 - \alpha^{3-D_e-D_f} \right]} \Sigma_{sw} \\ & + \frac{2}{r_{\max}} \frac{\phi(3 - D_e - D_f)}{\left(\tau_g^{\text{eff}}\right)^2 (D_e - D_f)} \frac{\left\{ 1 - \left[\alpha^{3-D_e-D_f} + S_u (1 - \alpha^{3-D_e-D_f}) \right]^{\frac{D_e-D_f}{3-D_e-D_f}} \right\}}{\left[1 - \alpha^{3-D_e-D_f} \right]} \Sigma_{iw}. \end{aligned} \quad (21)$$

Equation 21 is the electrical conductivity model for frozen saturated porous medium, which is similar to the theoretical model as developed by Luo et al. (2023). They deduced a physically-based model to show the variation of the electrical conductivity as a function of temperature considering the effect of liquid water saturation by using an unfrozen exponent. However, the phase transformation of liquid water not only affects the unfrozen water content, but also changes the tortuous length, thus we derive a novel electrical conductivity model considering the variations of the unfrozen water content and tortuous length below the freezing temperature.

To describe the soil water retention properties below the freezing temperature, and to neglect the effect of the parameters of the SFCC on the electrical conductivity of the unsaturated frozen porous medium, the residual water and adsorbed water contents were ignored in this study and we use the following expression (Wang et al., 2017),

$$S_u = \left\{ \frac{1}{\ln \left[e + \left(\frac{e^{(\sigma_0 - \tau)} }{a} \right)^b \right]} \right\}^c, \quad (22)$$

where a , b , and c represent the physically fitting parameters and are related to the volumetric fraction of micropores, meso-pores and macro-pores to the total pore volume of the porous medium.

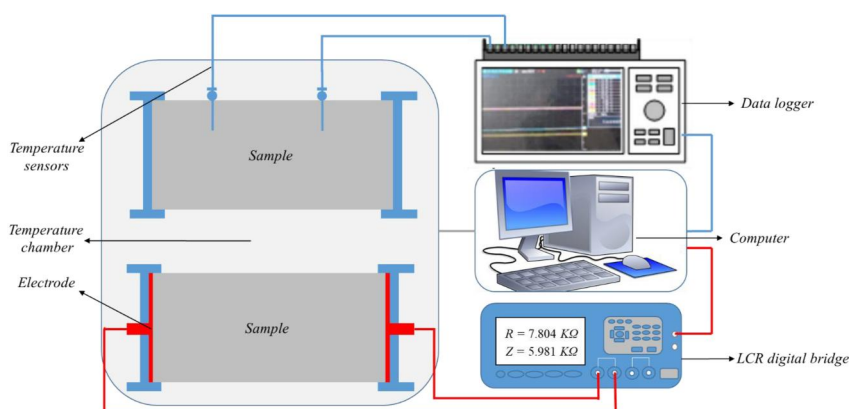


Figure 2. Laboratory experimental set-up for the electrical resistance experiments. It is composed of a LCR digital bridge and a temperature control system. The measurement system consists of the electrical resistance test unit of specimens and the temperature monitoring unit, and the temperature control system is a high-low temperature cycling experimental chamber.

4. Laboratory Experiments and Results

4.1. Experimental Setup

The electrical resistance measurements were conducted using the two-electrode method, which does not destroy the soil sample. The electrical conductivity can then be determined from the measured experimental values of the electrical resistance at a given temperature:

$$\sigma = \frac{L}{RS} = \frac{1}{K_g R}, \quad (23)$$

where R (in Ω) represents the experimental value of the electrical resistance; L (in m) and S (in m^2) represents the length and the area of the specimen, respectively. The geometrical factor $K_g = S/L$ (in m) is computed from the geometrical dimensions of the specimen.

A schematic diagram of the instrumentation for measuring the electrical resistance of frozen soils is described in Figure 2. It includes a sample temperature control device (i.e., an environmental chamber), a temperature measurement device, an electrical resistance measurement device (high-precision LCR digital bridge), electrodes and several electrode wires. The environmental chamber was provided to control the temperature of the specimen with a 0.1°C accuracy and a measurement range from 40 to -30°C . The high-precision LCR digital bridge with an accuracy of $10^{-4} \Omega$ (frequency variation range from 50 Hz to 100 kHz) was selected to measure the electrical resistance of specimens with a frequency of 100 Hz for ignoring the effects of the electrode polarization (low-frequency) and ice polarization (high-frequency) (Coperey, Revil, Abdulsamad, et al., 2019; Luo et al., 2023). The temperature measurement device records the soil specimen temperature with an accuracy of 0.5°C . The soil container is a transparent polypropylene cylinder with an inner diameter of 40 mm and a height of 90 mm, then a triaxial sample cavity is adopted for fixing the specimen container. To prevent the metallic components from affecting the electrical resistance of the specimens, we substituted them with plexiglass in the triaxial cavity. Copper electrode plates (40 mm diameter and 2 mm height) are applied as the measurement electrodes in addition to a set of copper wires.

Nuclear magnetic resonance method (NMR) has been proven efficient to determine the liquid water content in frozen state without disturbing the soil sample. To reduce the effect of bulk ice and consider the influence of the temperature, a real-time temperature control NMR apparatus (developed by Central South University, China and the Suzhou Niumag Analytical Instrument Corporation) was used to determine the unfrozen water saturation during the freezing processes.

The laboratory-based NMR method determines the liquid water content based on the inversion results of hydrogen signal values in different conditions (different initial conditions and temperatures) by measuring the free induction decay (FID) and the transverse relaxation time (e.g., Shen et al., 2020; Teng et al., 2020). This is

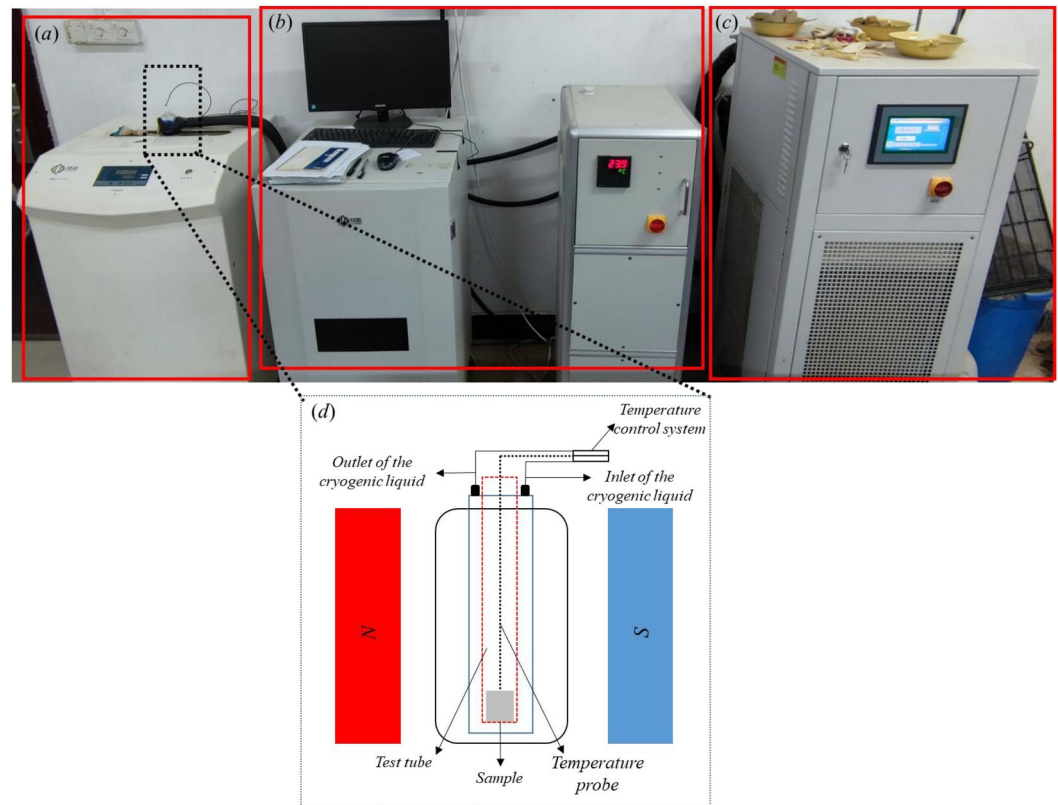


Figure 3. Schematic diagram of the experimental apparatus for unfrozen water content, which is named a temperature-controlled nuclear magnetic resonance (NMR) apparatus. It consists of a NMR measurement system (a), a data acquisition and analysis system (b), and a temperature-controlled system (c). (d) Schematic diagram of the temperature-controlled sample in the magnetic field.

mainly because the FID and the transverse relaxation time are proportional to the liquid water content of the sample. The NMR apparatus is presented in Figure 3. It includes a NMR system (Figure 3a), a temperature-controlled system (Figure 3c), a data acquisition system as well as an analysis system (Figure 3b). The NMR system consisted of a magnet unit, a sample tube and a radio frequency system (Figure 3d). To guarantee the stability and uniformity of the magnetic field, the temperature and frequency of the NMR magnet were kept at $30 \pm 0.01^\circ\text{C}$ and 12 MHz. The tube contains a column-shaped specimen cell with a height of 10 mm and a diameter of 9 mm, and a temperature probe is located in the sample to monitor a precise temperature. The cryogenic liquid is circulated and linked to the temperature control system, including a circulating pump and an air compressor, and they can be quickly cooled or heated to achieve a stable and effective temperature environment for the soil sample based on the comparison of the measured temperature and the target value in real time.

4.2. Materials and Test Conditions

Three types of soils are chosen as the test materials in these experiments: quartz sand, red clay and clayey silt (grain diameter of the specimens lower than 2 mm). The quartz sand is a commercial medium-coarse grained sand with the grain sizes ranging from 0.5 to 1 mm. A typical red clay was selected from Changsha (China), and the clayey silt was sampled at Beijing (China). The basic physical properties of the three samples are listed in Table 1.

In order to remove any mineral ions on the soil particles surface, the soils were first washed using distilled water, and the oven-dried soil materials were then blended with a certain amount of salt water (NaCl solution) at a specific salinity to produce samples with various initial water saturations. Soil material with a specific initial water content was then divided into three parts. The first part was compacted into the specimen cylinder to the target height with a dry density of 1.6 g/cm^3 , which is adopted to measure the electrical resistance of the soil specimen, then we placed a 2 mm graphite powder layer and a copper electrode plate at both ends of the soil

Table 1
Basic Physical Properties of the Specimens: Quartz Sand, Red Clay and Clayey Silt

Sample	Liquid limit (%)	Plastic limit (%)	Optimum water content (%)	Maximum dry density (g/cm ³)	Specific gravity	Porosity (ϕ)
Quartz sand	–	–	–	1.60	2.64	0.240
Red clay	36.02	21.5	16.2	1.73	2.73	0.40
Clayey silt	29.9	21.5	16.2	1.71	2.70	0.368

specimen. The second part was compacted into the specimen cylinder with a height of 90 mm and a dry density of 1.6 g/cm³, and a temperature sensor was inserted from the side port to the central axis of the soil column to monitor the temperature of the inner soil specimen and compare it with the target value in real time and both specimens were placed in the temperature control chamber. In addition, for the measurement of the unfrozen water saturation as a function of temperature, the third soil sample was inserted in a sample tube of 9 mm in diameter and 10 mm in height with a dry density of 1.6 g/cm³ and placed in the NMR field system. The temperature of the NMR sample tube was precisely regulated, and subject to a freezing cycle. During the electrical resistance and NMR measurements, the temperature was reduced in a stepwise manner with about 12 different temperature points in the range of 298–255 K. For temperature stability during the measurements, each temperature was held for 4 hr. Once the sample temperature stabilized, the electrical resistance of the sample was measured at that temperature. This allowed for the determination of the electrical conductivity, in accordance with Equation 23. Besides, we also measured the value of the FID for NMR experiments at the corresponding temperature, so the unfrozen water saturation could be calculated based on the relationship of FID with liquid water content (Teng et al., 2020).

Six cases of soil columns were designed to investigate the electrical properties of unsaturated frozen soils with temperature, initial water content and ionic concentration, as listed in Table 2. Cases 1, 3 and 5 were conducted to study the effects of the variable initial water content on the electrical conductivity and unfrozen water saturation in different kinds of soils, and the initial ionic concentration was controlled at 0.180 mol/L. Different initial ionic concentrations in cases 2, 4 and 6 were designed to investigate their effect on the unfrozen water saturation and electrical conductivity with quartz sand, red clay and clayey silt, and the initial water saturation of samples was controlled at 0.670, 0.800 and 0.870, respectively.

4.3. Experimental Results

The measurement results for the various soil types (quartz sand, red clay and clayey silt) at different initial water contents are shown in Figure 4, which presents the variations of electrical conductivity and unfrozen water saturation with temperature. For the three different samples, there are two stages in the electrical conductivity change with temperature: a slight linear decline stage followed by a phase of rapid decline on a semi-logarithmic scale in the electrical conductivity range below the freezing temperature. Figures 4a–4c also shows that the electrical conductivity increases with increasing initial water saturation in the entire temperature range. The decrease of the water saturation leads to a stronger decrease of the electrical conductivity for red clay and clayey silt above the freezing temperature than below. Based on the obtained SFCC, as shown in Figures 4d–4f, the unfrozen water content remains more and less the same regardless the initial saturation, while the difference in

Table 2
Test Conditions

Case	Type	Dry density (g/cm ³)	Initial water saturation	Initial ionic concentration (mol/L)	Temperature range (K)
1	Quartz sand	1.60	1.00, 0.80, 0.67, 0.47	0.180	255–298
2	Quartz sand	1.60	0.67	0.046, 0.180, 0.570	255–298
3	Red clay	1.60	1.00, 0.80, 0.60, 0.40	0.180	255–298
4	Red clay	1.60	0.800	0.092, 0.180, 0.570	255–298
5	Clayey silt	1.60	1.00, 0.87, 0.65, 0.43	0.180	255–298
6	Clayey silt	1.60	0.870	0.046, 0.180, 0.570, 1.240	255–298

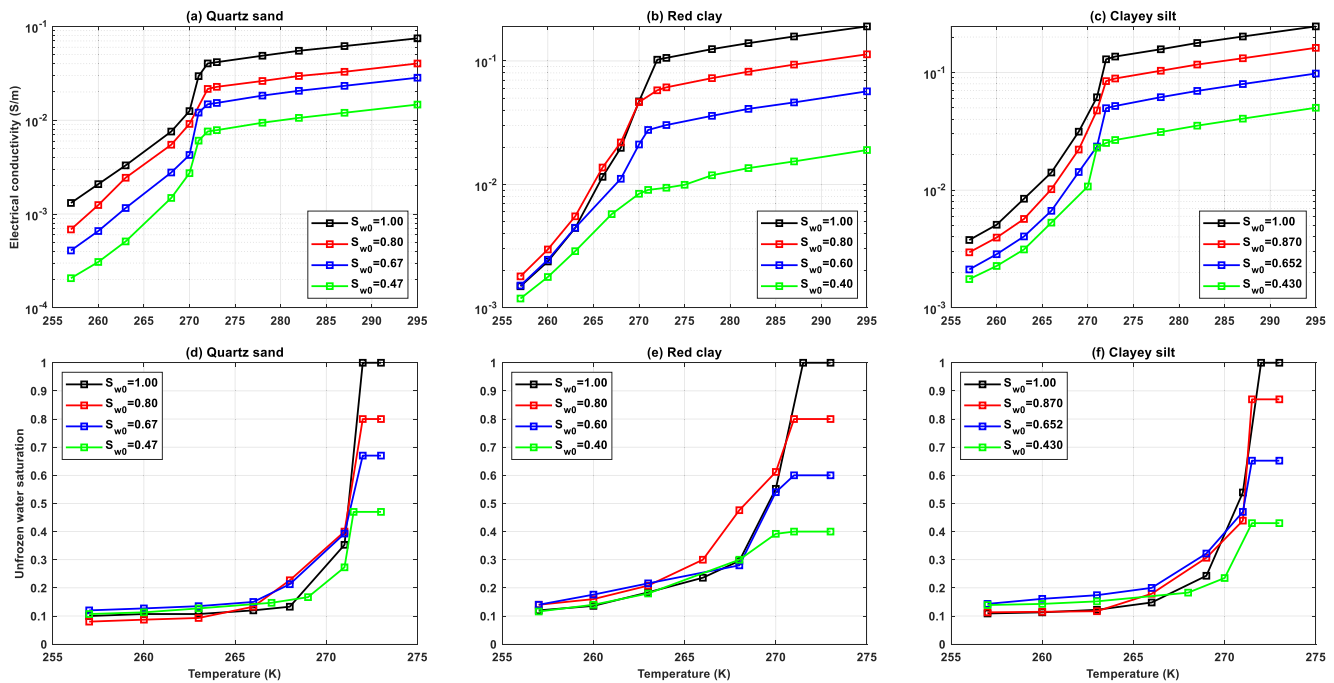


Figure 4. Experimental data for different initial water saturations, electrical conductivity is measured by electrical conductivity experiment and unfrozen water saturation is measured by nuclear magnetic resonance method (initial concentration is 0.180 mol/L): (a–c) the experimental data of electrical conductivity with three kinds of samples (quartz sand, red clay and clayey silt, respectively); (d–f) the experimental data of unfrozen water saturation with three types of samples (quartz sand, red clay and clayey silt, respectively).

ionic concentration is large. Therefore, the ionic concentration dominates the variation in the electrical conductivity of unsaturated frozen soils for different initial water contents.

Figure 5 describes the effect of the different initial ionic concentrations on the electrical conductivity and unfrozen water saturation for the various soil types. With the decrease of the temperature, the electrical conductivities first start to linearly decrease on a semi-logarithmic scale in the electrical conductivity range until they reach a threshold below the freezing temperature below which they decrease rapidly. Additionally, the experimental results presented in Figure 5 show that the unfrozen water saturation increases with an increase of the initial salt concentration in the entire temperature range, indicating a strong influence of the salt concentration on the pore water in freezing process. It can also be seen that over the entire temperature range, the electrical conductivity rises with increasing salt concentration. Therefore, for different initial salt concentrations, a higher ionic concentration results in a higher unfrozen water saturation. The electrical conductivity of unsaturated frozen porous medium is primarily influenced by the ionic concentration.

5. Results and Discussion

5.1. Model Calculation Procedure

The electrical conductivity of partially saturated porous media can be predicted in accordance with the flow chart presented in Figure 6 above the freezing temperature. First, we determine the pore water conductivity σ_w from Equation 10, the specific surface conductances in the mineral surface-water interface Σ_{sw} and air-water interface Σ_{aw} based on the surface complexation model at a given temperature and based primarily on the ionic concentration (see Appendices A and C). Then, the predicted value of the electrical conductivity σ is determined by Equation 20 using representative values of fractal PSD parameters r_{max} , α , D_f and D_e . The model parameters are fitted to the experimental data using the least-squares algorithm, through the use of the mean absolute percentage error (MAPE) to evaluate the performance of the proposed model. Note that MAPE is a relative error measure used to compare the predictive accuracy of the proposed model (e.g., Rembert et al., 2020).

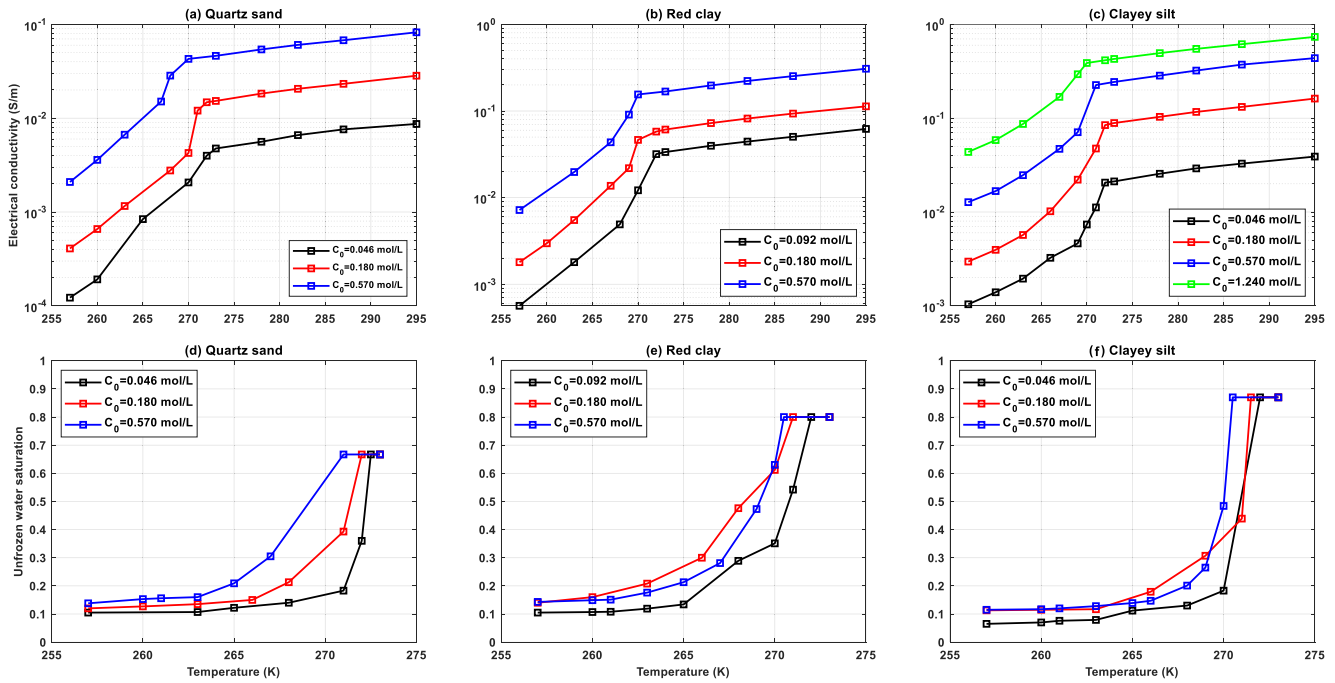


Figure 5. Experimental data for different initial salt concentrations, electrical conductivity is measured by electrical conductivity experiment and unfrozen water saturation is measured by nuclear magnetic resonance method (initial water saturation of quartz sand, red clay and clayey silt is 0.670, 0.800, and 0.870, respectively): (a–c) the experimental data of the electrical conductivity with different types of soils (quartz sand, red clay and clayey silt, respectively); (d–f) the experimental data of the unfrozen water saturation with different types of soils (quartz sand, red clay and clayey silt, respectively).

Figure 6 describes the flow chart also used to predict the electrical conductivity of unsaturated frozen porous media. First, we obtain the unfrozen water saturation $S_u(T)$ and the ionic concentration $C_u(T)$ below the freezing temperature. Second, the pore water conductivity $\sigma_w(T)$ and the specific surface conductance of the mineral surface-water Σ_{sw} , the bulk ice-water Σ_{iw} and the air-water Σ_{aw} interfaces were determined by using the surface complexation model. Third, the predicted value of the electrical conductivity is obtained based on Equation 19 using representative values of fractal distribution parameters of r_{max} , α , D_f and D_e . Therefore, the SFCC model (unfrozen water saturation) comprises three physical parameters: a , b , and c , while the electrical conductivity model involves four parameters: r_{max} , α , D_f and D_e . We determine the values of these parameters for each core

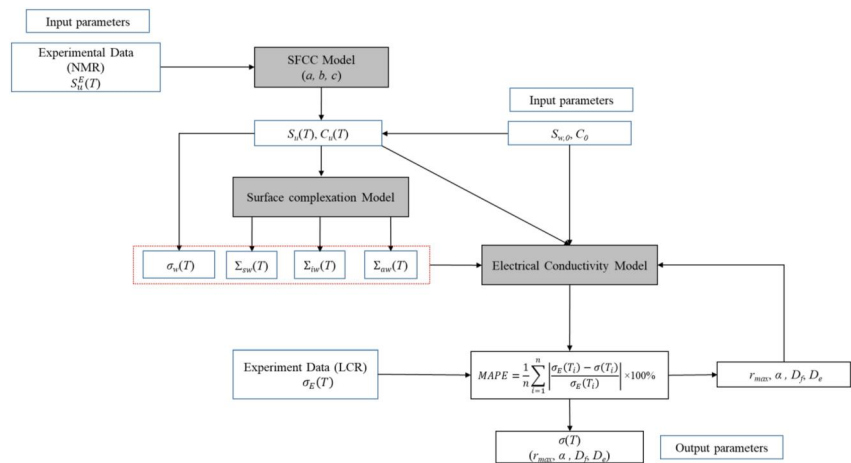


Figure 6. Numerical procedure to compute the proposed physically-based model of electrical conductivity for unsaturated porous media from $S_{w,0}$, C_0 , $S_u(T)$, $C_u(T)$ and microstructural parameters of the proposed model (r_{max} , α , D_f and D_e), where the (T) and $\sigma_E(T)$ represent the experimental data of the unfrozen water saturation and electrical conductivity at freezing temperature, respectively.

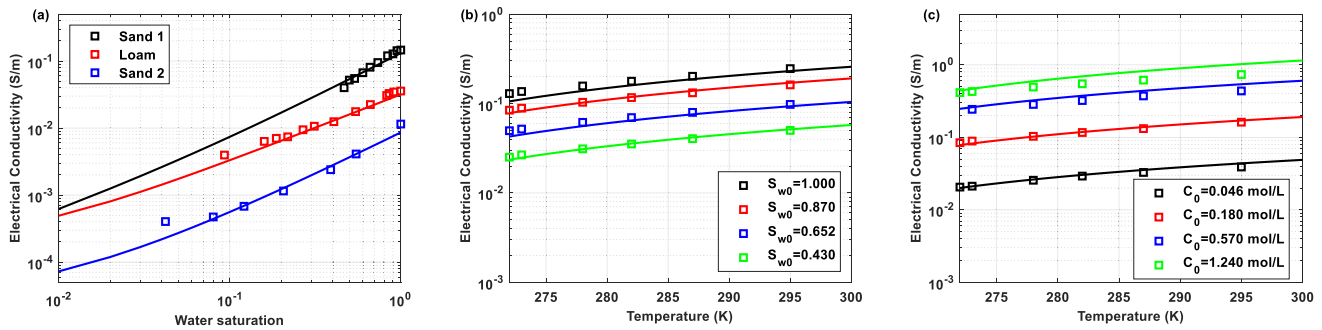


Figure 7. (a) Variation of electrical conductivity as a function of water saturation for different samples: Sand 1 (from Weerts et al., 1999), Loam (from Doussan & Ruy, 2009), and Sand 2 (from Breede et al., 2011). (b) Predicted dependence of electrical conductivity on temperature and water saturation above freezing temperature. The symbols are the experimental data of electrical conductivity as measured in this study for clayey silt, and the solid lines are predicted from Equation 20 with fractal distribution. (c) Predicted dependence of electrical conductivity on temperature for different initial ionic concentrations above freezing temperature, and the experimental data (symbols) of electrical conductivity as measured in this study for clayey silt. The solid lines are predicted from Equation 20 with fractal distribution, and the best fit parameters of fractal pore size distribution and the mean absolute percentage error values are shown in Table S2 in Supporting Information S1.

sample using the least-squares algorithm, including both the SFCC model and the conductivity model. We solve a nonlinear optimization program that optimizes parameter values using the MAPE.

5.2. Comparison With Experimental Data Under Partially Saturated Conditions

In this section, we compare the predicted results above the freezing temperature with published data in the literature and the experimental data acquired in this study. Figure 7a shows the water saturation dependence of the electrical conductivity of porous medium under partially saturated conditions. The predicted parameters of the proposed model with the results of the MAPE are presented in Table S2 in Supporting Information S1. Interestingly, we note that the proposed model (Equation 20) is in pretty good agreement with experimental data from the literature. Note that the proposed model (Equation 20) is an extension of the physically-based model developed by Jougnot et al. (2010) and Revil et al. (2007). We assume that the bulk conductivity is equal to the conductivity of the bulk solution used to saturate the sample in this study, which means we neglect the contribution of the counterions at the diffuse layer to the bulk conduction, and we consider the influences of the Stern layer and diffuse layer to the surface conduction at the mineral surface. Thus, the surface tortuosity depends solely on the solid phase and is independent of the water phase (water saturation) in this work.

In order to test the dependence of electrical conductivity on temperature, water saturation and ionic concentration, we plot the electrical conductivity as a function of temperature (T) for values ranging from 273 to 298 K for different water saturations and salinities in Figures 7b and 7c. The fitting parameters and the MAPE values are shown in Table S2 in Supporting Information S1. The low MAPE values show that the proposed model is well suited for reproducing experimental data on electrical conductivity in an unsaturated porous medium. We also observe that the electrical conductivity rises with temperature, water saturation and ionic concentration, which can be explained by the fact that ionic mobilities decrease when temperature declines, and the bulk electrical conduction decreases when ionic concentration, water saturation, and temperature decrease.

5.3. Comparison With Experimental Data of Fully Saturated Frozen Porous Media

The electrical conductivity of frozen porous medium for fully saturated conditions has been discussed in Coperey, Revil, Abdulsamad, et al. (2019) and Luo et al. (2023). Therefore, in this section, we address the capability of the proposed model (Equation 21) to predict the electrical conductivity with respect to experimental data in the complete temperature range (255–300 K) for different samples from Coperey, Revil, Abdulsamad, et al. (2019), Duvillard et al. (2021), and Luo et al. (2023). We plot the electrical conductivity of fully saturated frozen porous medium versus temperature over this entire temperature range as shown in Figure 8. The fitting parameters of the proposed model are listed in Table S3 in Supporting Information S1, and the MAPE is chosen to evaluate the performance for Equation 21, their values also are listed in Table S3 in Supporting Information S1. As indicated by low MAPE values, it illustrates that the proposed model is in large agreement with the trend of the experimental data.

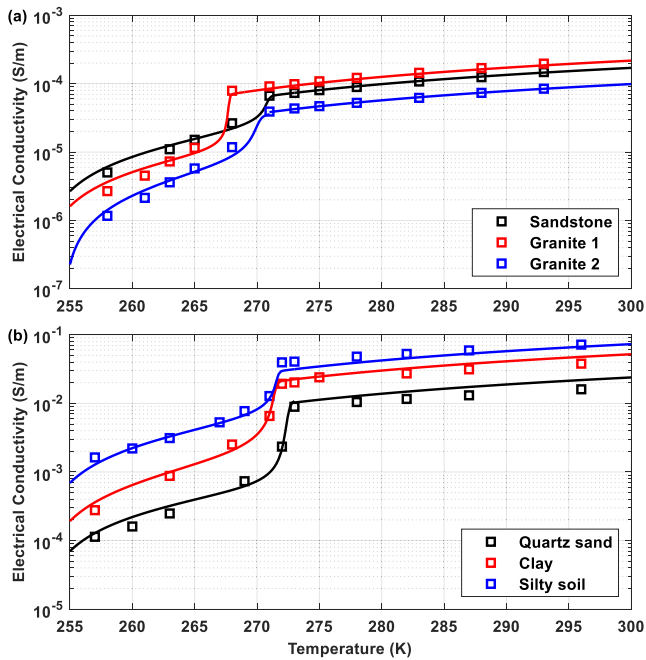


Figure 8. Evolution of electrical conductivity (σ) with temperature over the entire temperature range under fully saturated conditions. Experimental data are taken from Coperey, Revil, Abdulsamad, et al. (2019), Duvillard et al. (2021), and Luo et al. (2023). The symbols represent the experimental data of electrical conductivity for different samples, and the solid lines represent the computed results predicted from Equation 21 with fractal pore size distribution. The best estimated parameters of soil freezing characteristic curve and electrical conductivity models are shown in Table S3 in Supporting Information S1.

Obviously, as shown in Figure 8a, the proposed model can also predict the evolution of the freezing point for different saturated porous media (a threshold with the temperature). The transition point is located at about 268 K for the sandstone, and about 271 K for the granites, which is consistent with the experimental data from Coperey, Revil, Abdulsamad, et al. (2019) and Duvillard et al. (2021). As illustrated in Figure 8b, when exposed to positive temperature conditions, variations in the electrical conductivity for various soil samples with identical initial conditions (including salinity and water saturation) can be attributed to the influence of their PSD, characterized by fractal distributions of pore size (D_p) and capillary tortuosity (D_e). However, when the temperature drops below the freezing point, variations in the physical properties of soils lead to variations in unfrozen water saturation. Consequently, this results in disparities in ionic concentrations within soil pores. Thus, under sub-zero temperature conditions, distinctions in the electrical conductivity among different soil types are not solely dependent on their PSD but also on their overall physical properties, including unfrozen water saturation and salinity.

5.4. Comparison With Previous Models for Fully Saturated Frozen Porous Media

To better verify the applicability of the proposed model, two existing petrophysical models of electrical conductivity proposed by Coperey, Revil, Abdulsamad, et al. (2019) and Luo et al. (2023) are used to be compared with the new theoretical model (Equation 21) in this study. Figure 9 shows the comparison of the electrical conductivity as a function of temperature between the experimental data (symbols) from the literature and predicted results from Equation 21 (black line), and from the theoretical models established by Coperey, Revil, Abdulsamad, et al. (2019) (red line) and Luo et al. (2023) (blue line). The fitting parameters of the corresponding models are obtained in Table S4 in Supporting Information S1. The MAPE is chosen

to assess the performance of the different physically-based models, their values are also listed in Table S4 in Supporting Information S1.

Figure 9 illustrates that the proposed model correctly reproduces the tendencies of the experimental data from Coperey, Revil, Abdulsamad, et al. (2019) and Luo et al. (2023) with low MAPE values, which are 0.070, 0.110, and 0.123 for the granite, the silty soil ($C_0 = 0.046$ mol/L), and the silty soil ($C_0 = 0.180$ mol/L), respectively. Compared with the predicted values of previous models, it shows that the proposed model in this study performs better than other existing models considering the effect of the ice formation at the pore scale on the electrical conductivity of fully saturated frozen porous medium.

Considering the effect of the unfrozen water content, Coperey, Revil, Abdulsamad, et al. (2019) established a dynamic Stern layer model using a volume averaging method accounting for the bulk conduction and the surface conduction in the mineral-water interface, which is given by

$$\sigma = \phi S_u(T) \{ \phi \sigma_w(T) + \rho_g [B(T) - \lambda(T)] \text{CEC} \}, \quad (24)$$

where ρ_g represents the grain density (kg m^{-3} , usually $\rho_g = 2,650 \text{ kg m}^{-3}$), $B(T)$ ($\text{in m}^2 \text{ s}^{-1} \text{ V}^{-1}$) is the apparent mobility of the counterions as a function of temperature for surface conduction ($B(\text{Na}^+, 298 \text{ K}) = 3.1 \times 10^{-9} \text{ m}^2 \text{ s}^{-1} \text{ V}^{-1}$), $\lambda(T)$ ($\text{in m}^2 \text{ s}^{-1} \text{ V}^{-1}$) is the apparent mobility of the counterions as a function of temperature for the polarization ($\lambda(\text{Na}^+, 298 \text{ K}) = 3.0 \times 10^{-10} \text{ m}^2 \text{ s}^{-1} \text{ V}^{-1}$) (Revil et al., 2017), and the temperature dependence of $B(T)$ and $\lambda(T)$ can be obtained. CEC represents the cation exchange capacity (C/kg, or meq/100 g, with $1 \text{ meq}/100 \text{ g} = 963.20 \text{ C}/\text{kg}$). Therefore, we can determine the values of $\sigma_w(T)$ and $S_u(T)$ using Equations 10 and 22, respectively. The values of CEC for different samples can be obtained from the experiment (for granite, Coperey, Revil, Abdulsamad, et al., 2019) and as fitting parameters (for silty soil) of Equation 24.

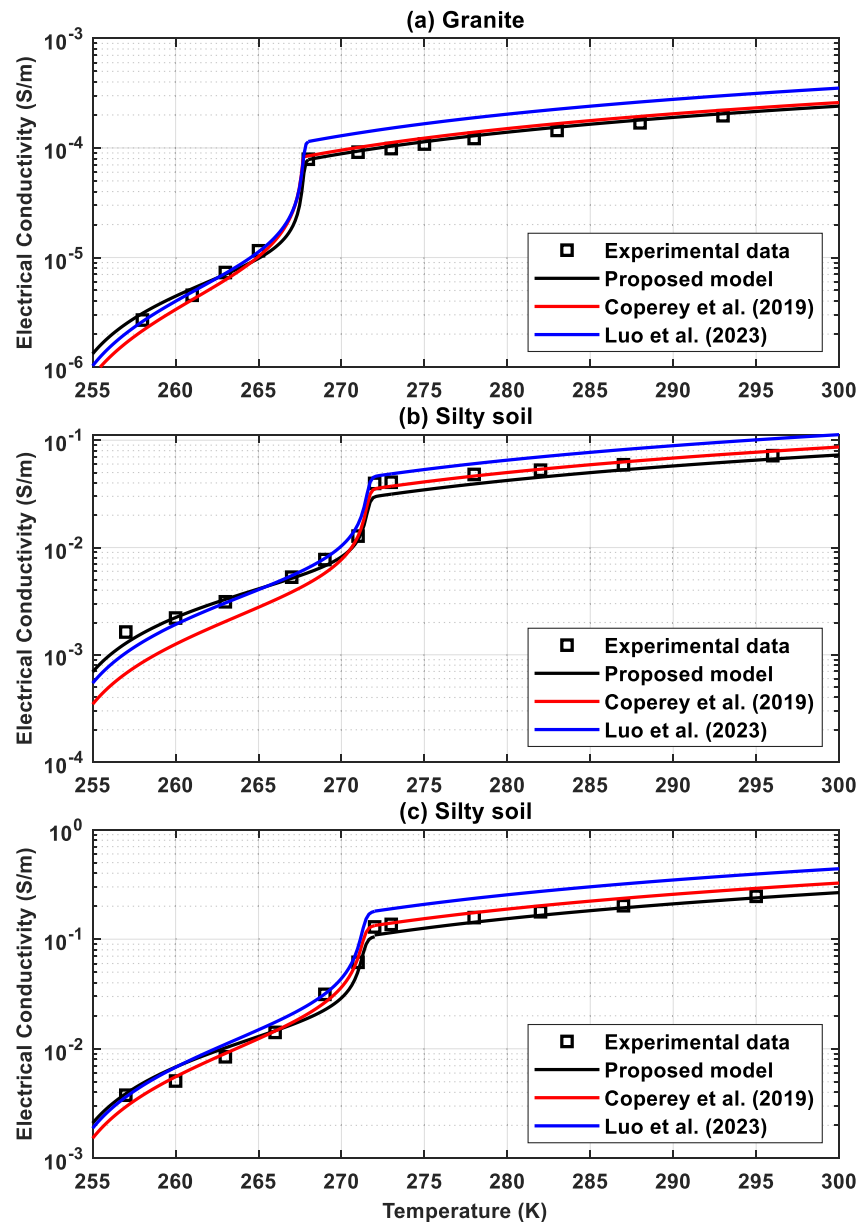


Figure 9. The comparison of electrical conductivity as a function of temperature between the experimental data and the predicted results: (a) Granite (from Coperey, Revil, Abdulsamad, et al., 2019); (b) Silty soil ($C_0 = 0.460$ mol/L, from Luo et al., 2023); (c) Silty soil ($C_0 = 0.180$ mol/L, from Luo et al., 2023). Black symbols depict the measured data of Coperey, Revil, Abdulsamad, et al. (2019) and Luo et al. (2023). Black line illustrates the predicted results of the proposed physically-based model, red line illustrates the predicted results of the Coperey, Revil, Abdulsamad, et al. (2019) model, and blue line represents the behavior predicted by Luo et al. (2023) model. The basic physical properties of samples and the parameters of soil freezing characteristic curve model are shown in Table S3 in Supporting Information S1. The fitting parameters of these models and mean absolute percentage error values are listed in Table S4 in Supporting Information S1.

Figure 9 shows the predicted results of electrical conductivity as a function of temperature from Equation 24. The CEC values are taken 0.78 meq/100 g and 1.60 meq/100 g for granite and silty soil, respectively. The MAPE values of Coperey, Revil, Abdulsamad, et al. (2019) model are 0.129, 0.192, and 0.139 for the granite, the silty soil ($C_0 = 0.046$ mol/L), and the silty soil ($C_0 = 0.180$ mol/L), respectively (Table S4 in Supporting Information S1). The predicted results agree well with the experimental data above the freezing temperature. However, in frost states, because it ignores the effect of the liquid water transformation on the tortuosity and the contribution of the surface conduction at the bulk ice-water interface, the theoretical model established by Coperey, Revil, Abdulsamad, et al. (2019) results to lower predicted values than the proposed model below the freezing point.

In contrast, in order to consider the effects of the different PSDs and the surface conduction in the bulk ice-water interfaces, Luo et al. (2023) proposed a capillary bundle model for electrical conductivity as a function of temperature accounting for the surface complexation model and the Gibbs-Thomson expression,

$$\sigma = \frac{\phi S_u^n}{\tau^2} \sigma_w + \frac{2\phi(2 - D_f)\{1 - \alpha^{1-D_f}\}}{\tau^2(1 - D_f)r_{\max}(1 - \alpha^{2-D_f})} \Sigma_{sw} + \frac{2\phi(2 - D_f)(r_{\max}^{1-D_f} - r_i^{1-D_f})}{\tau^2(1 - D_f)r_{\max}^{2-D_f}(1 - \alpha^{2-D_f})} \Sigma_{iw}. \quad (25)$$

In their classical work with fractal PSD, an empirical parameter (unfrozen exponent, n) was defined in Luo et al. (2023). Figure 9 shows the predicted results of electrical conductivity as a function of temperature from Equation 25. The unfrozen exponent n is 2.00 and 1.60 for granite and silty soil, respectively. The MAPE values of Luo et al. (2023) model are 0.361, 0.206, and 0.352 for the granite, the silt soil ($C_0 = 0.046$ mol/L), and the silty soil ($C_0 = 0.180$ mol/L), respectively (Table S4 in Supporting Information S1). We can observe from Figure 9 that the predicted results are in high agreement with the experimental data below the freezing temperature. However, because of the heterogeneity of the capillaries, the predicted results of Luo et al. (2023) deviate significantly from the published data above the freezing temperature. The phase transformation of the pore water not only affects the connectivity of the capillaries, but also the tortuous length, which in turn influences the changes in bulk and surface conductions. Consequently, the fractal dimension (D_e) of capillary tortuosity is recognized as a physical exponent for the effect of the phase transition in this study and provides a rigorous physical relation between the tortuous length and the electrical conduction. Therefore, when comparing the theoretical approaches proposed in this study to the models of Coperey, Revil, Abdulsamad, et al. (2019) and Luo et al. (2023), we conclude that in the proposed model (Equation 21), the prediction of the electrical conductivity has a higher accuracy than in the previous models.

5.5. Comparison With Experimental Data of Unsaturated Frozen Porous Media

To evaluate the performance of the proposed electrical conductivity model (Equation 19), experimental electrical conductivity data for different types of soil samples (quartz sand, red clay and clayey silt) were selected for different initial water saturations. The basic properties of the samples are listed in Table 1. We fit the parameters of the SFCC model based on the experimental data acquired using the NMR method (Table S5 in Supporting Information S1). The comparison between the predicted results of the proposed model from Equation 19 and the experimental data with different initial water saturations over the entire temperature range is shown in Figure 10. The estimated parameters and the calculated MAPE values of the proposed model are mentioned in Table S5 in Supporting Information S1.

Figure 10a shows the comparison between the electrical conductivity predicted by the proposed model and the experimental data for quartz sand with different initial water saturations. MAPE values in the entire temperature range were 0.062, 0.114, 0.133, and 0.198 for various initial water saturations, respectively. As shown, the physically-based model established in this study can predict the relationship of electrical conductivity versus temperature of unsaturated frozen porous medium over a complete temperature range. Moreover, we observe that the electrical conductivity linearly decreases with temperature above the freezing temperature of the frozen porous medium ($T > T_m$), whereas the electrical conductivity rapidly falls with temperature when $T < T_m$. As shown in the comparison between predicted results and experimental data for quartz sand, the freezing temperature declines with initial water saturation, as liquid water retreats to dramatically smaller capillaries, as determined in the Young-Laplace effect (Equation 4). Therefore, as formulated in the Gibbs-Thomson effect (Equation 5), smaller pores filled with liquid water lead to a lower freezing temperature for unsaturated frozen porous medium. We also observe from Table S5 in Supporting Information S1 that the fractal dimensions of pore size (D_f) and capillary tortuosity (D_e) remain stable with the entire water saturation range. This is mainly due to the fact that D_f and D_e are sensitive to the basic physical properties of the porous medium, such as the porosity, the maximum and minimum pore radii of the REV. However, they are not affected by the initial state of the porous medium, for instance, the initial water saturation, as shown in Table S5 in Supporting Information S1.

Figures 10b and 10c describe similar characteristics for red clay and clayey silt. As indicated by the small MAPE values, the predicted results of the proposed model agree well with the experimental data of red clay and clayey silt. Comparing to Figure 10a, we observe that the electrical conductivity of red clay or clayey silt is larger than

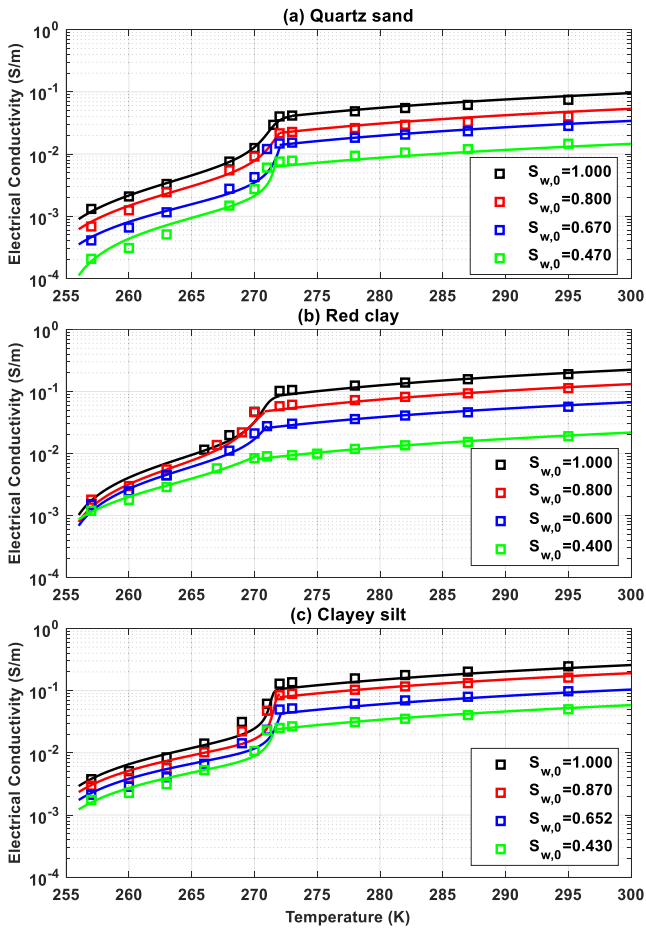


Figure 10. Evolution of electrical conductivity (σ) as a function of temperature with different initial water saturations for three types of unsaturated frozen soils. Symbols are the experimental data of the electrical conductivity measured in this study and solid lines are the predicted results by the new proposed fractal model, and initial salt concentration for these soil samples was set to 0.180 mol/L. (a) Quartz sand; (b) Red clay; (c) Clayey silt. The best estimated parameters of the soil freezing characteristic curve and the electrical conductivity model are given in Table S5 in Supporting Information S1.

that of quartz sand, and that their freezing temperature is lower than that of quartz sand for the same initial water saturation.

In order to validate the characteristics of the proposed electrical conductivity model for different initial ionic concentrations and different types of soil samples (quartz sand, red clay, and clayey silt). We calculated the evolution of electrical conductivity as a function of temperature with various salinities based on Equation 19. Figure 11 depicts the comparison between the predicted results from the proposed model and the experimental data for various initial ionic concentrations. The model parameters in this proposed model and the MAPE values are given in Table S6 in Supporting Information S1. It can be noted that the predicted results of the proposed model are in good agreement with the experimental data for varying salinities. The unfrozen water saturation and electrical conductivity increase with the increase of initial salinity. Furthermore, we observe that the higher salinity enhances the freezing temperature depression of soil samples, as the salt affects the soil-water activity. The fractal dimensions of pore size (D_f) and capillary tortuosity (D_e) are also not sensitive to the initial salinity for a full range of ionic concentrations from Table S6 in Supporting Information S1. Overall, the predictions of the proposed models and the experimental data from the literature and this study illustrate that our new physically-based model can correctly reproduce the tendencies of the electrical conductivity of partially saturated frozen porous media in the entire temperature range and salinity range.

5.6. Formation Factor

In this section, we explore the dependence of the apparent formation factor on porosity and water saturation, based on Equations D1 and D2. In this proposed model, the apparent formation factor is sensitive to the fractal dimension of pore size (D_f) and the fractal dimension of capillary tortuosity (D_e). Figure 12a compares the predicted formation factor with experimental data from the literature. The symbols correspond to the experimental data from the Clean sandstone (Revil et al., 2017) and Fontainebleau sandstones (Revil et al., 2014), while the solid line is the estimated results from Equation D1. As shown, the fitted results of the proposed model and experimental data provide with similar tendencies, and the fitting parameters of the proposed model are shown in Table S7 in Supporting Information S1. Additionally, the formation factor linearly decreases on a log-log scale with the increase of porosity, which is highly consistent with findings from the literature (Revil et al., 2017).

Moreover, we also test our new model for describing the variation of the apparent formation factor as a function of water saturation against data sets of sandy clay (Revil, Soueid Ahmed, & Matthai, 2018) in Figure 12b. The black symbols and the solid line are the experimental data and the predicted results of the formation factor from Equation D1, respectively. The red symbols and the dashed line are the experimental data and the predicted results of the apparent formation factor from Equation A2, respectively. As shown in Figure 12b, the proposed model is able to reproduce the experimental data. We also observe that the formation factor is independent of water saturation whereas the apparent formation factor nonlinearly declines when the water saturation increases, due to the fact that more pores are saturated by water (i.e., more pores contribute to the total electrical conduction).

We go one step further to explore the dependence of the apparent formation factor on the temperature using Equation D3. The apparent formation factor is defined as the ratio of the actual pore water conductivity to the electrical conductivity of porous medium in this study. To evaluate the performance of the apparent formation factor model in frozen porous media, we compare the prediction results of this model with the experimental data from Coperey, Revil, Abdulsamad, et al. (2019). The fitting parameters of this model are shown in Table S7 in

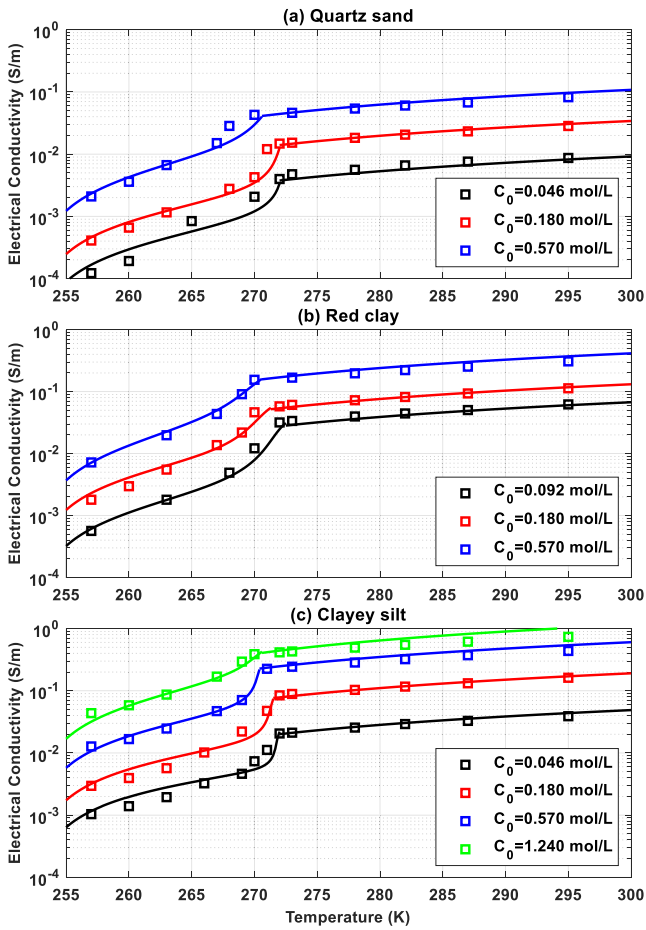


Figure 11. Evolution of electrical conductivity as a function of temperature with different initial salt concentrations for three types of unsaturated frozen soils. Symbols are the experimental data of the electrical conductivity as measured in this study and the solid lines are the predicted results by predicted by the fractal pore size distribution model (Equation 19). (a) Quartz sand, initial water saturation 0.670. (b) Red clay, initial water saturation 0.800. (c) Clayey silt, initial water saturation 0.870. The best estimated parameters of the soil freezing characteristic curve and the electrical conductivity model are given in Table S6 in Supporting Information S1.

Supporting Information S1. As shown in Figure 13, our model can reproduce the experimental data. Besides, the apparent formation factor remains constant above the freezing temperature and exhibits no temperature dependence, as it is solely determined by porosity and tortuosity. However, it experiences a sharp increase below the freezing temperature due to its heightened sensitivity to unfrozen water saturation.

5.7. Model Features Analysis and Discussion

The proposed temperature-dependent conductivity model is associated with the unfrozen water saturation in partially saturated frozen porous media, especially in terms of bulk conduction. To better understand how the physical parameters in the empirical SFCC model affect the electrical conductivity, a sensitivity analysis of the proposed model (Equation 19) was conducted for varying modeling parameters (a , b , and c) over wider ranges. Figure 14 shows the influence of these physical parameters on the electrical conductivity. As shown in Figure 14a, the freezing temperature on the electrical conductivity versus temperature curve (σ - T curve) decreases with the increase in a . The larger a value indicates the macro-pores in the soil sample become smaller, and the volumetric proportion of small pores increases, resulting in a lower freezing temperature according to Equation 5 (Wang et al., 2017). Moreover, it is noteworthy that a exclusively affect the phase characterized by a rapid decline in electrical conductivity with temperature, whereas the stages involving linear decrease and slight decline (residual stage) exhibit no sensitivity to this parameter.

Additionally, Figures 14b and 14c illustrate that electrical conductivity increases with the decline of physical parameters b and c below the freezing temperature, while the freezing temperature of the soil sample shows no sensitivity to these parameters. This is because that physical parameters b and c have minimal effect on the size of the macro-pores (Wang et al., 2017). Besides, as parameter c increases, the volume proportion of micro-pores in the soil sample decreases. In contrast, changes in parameter b have a smaller impact on the volume proportion of micro-pores (Wang et al., 2017). When the temperature decreases in the soil sample, liquid water in the large pores transforms into solid ice, while the liquid water remains in small pores. Therefore, in the relationship between the electrical conductivity and temperature (σ - T curve) of unsaturated frozen porous media, the influence of

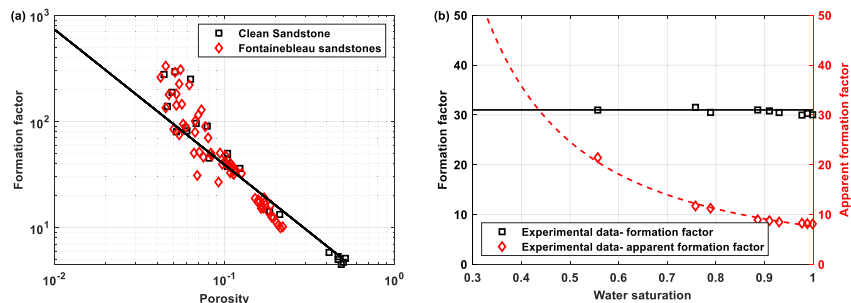


Figure 12. (a) Evolution of the formation factor as a function of porosity (solid line, Equation D1). The data set of experimental data are taken from Revil et al. (2017, Clean sandstone), Revil et al. (2014, Fontainebleau sandstones); (b) Evolution of the (apparent) formation factor as a function of water saturation-Equations D1 and D2. The experimental data are taken from Revil, Soueid Ahmed, and Matthai (2018, Sandy clay). The best fit parameters of fractal pore size distribution are shown in Table S7 in Supporting Information S1.

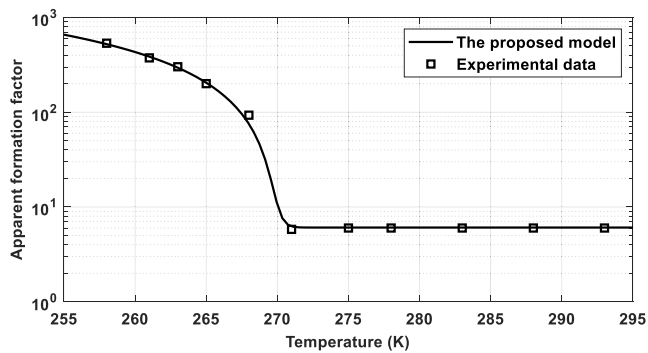


Figure 13. Evolution of the apparent formation factor as a function of temperature—Equation D3. The symbols are taken from Coperey, Revil, Abdulsamad, et al. (2019) and calculated by the proposed model (solid line). Model parameters are given in Table S7 in Supporting Information S1.

physical parameter c on the electrical conductivity with temperature variation is greater than that of parameter b .

The temperature-dependent electrical conductivity model proposed in this study includes four geometric parameters related to pore size (r_{\max} , α , and D_f) and pore tortuosity (D_e). In accordance with the geometric parameter ranges obtained by the least squares algorithm in this study, a sensitivity analysis of the proposed model (Equation 19) was carried out using the representative values of the involved parameters as shown in Figure 15. The response of the electrical conductivity with temperature to the variation of the maximum pore radius (r_{\max}) is described in Figure 15a. The maximum pore radius r_{\max} only affects the electrical conductivity below the freezing point, but has little effect on it above the freezing temperature. This implies that the contribution of bulk conduction to the total electrical conductivity is greater than that of surface conduction above the freezing temperature. However, when the temperature drops below the freezing point, liquid water transforms into solid ice in the pore spaces, leading to a decline in the bulk conduction. Moreover, a larger

r_{\max} value results in lower surface conductivity (Equation 19), consequently leading to a lower electrical conductivity, as illustrated in Figure 15a.

Figures 15b and 15c describe the influence of α and D_f on electrical conductivity. It is important to note that electrical conductivity increases with an increase in D_f or a decrease in α . The reason is that, when D_f increases or α decreases, the total number of capillaries with relatively small radii at the REV scale rises, thereby increasing the surface conductivity of the frozen soil sample. Consequently, the total electrical conductivity also increases. Note that in porous materials, surface conductivity is predominantly influenced by the contribution from smaller capillaries, assuming constant surface conductance and pore water conductivity. As shown in Figure 15d, an increase in the fractal dimension of pore tortuosity (D_e) leads to higher flow resistance, which significantly impacts the electrical conductivity of unsaturated frozen porous media, resulting in a decline in the total electrical conductivity.

The proposed conductivity model in this study illustrates the evolution of electrical conductivity with temperature for different types soil samples, which consists of three SFCC modeling parameters (a , b , and c) and four geometric parameters related to pore size (r_{\max} , α , and D_f) as well as pore tortuosity (D_e). The SFCC modeling parameters can be determined by fitting the experimental unfrozen water saturation data. It is worth noting that these parameters are not only related to the pore volumetric contents of the pore size (C. Wang et al., 2017), but also related to the initial conditions of the porous media (i.e., water saturation and salinity), as shown in Tables S5 and S6 in Supporting Information S1.

The remaining geometric parameters in temperature-dependent electrical conductivity model can be determined by fitting the experimental electrical conductivity data with varying temperature. In the case of quartz sand in this

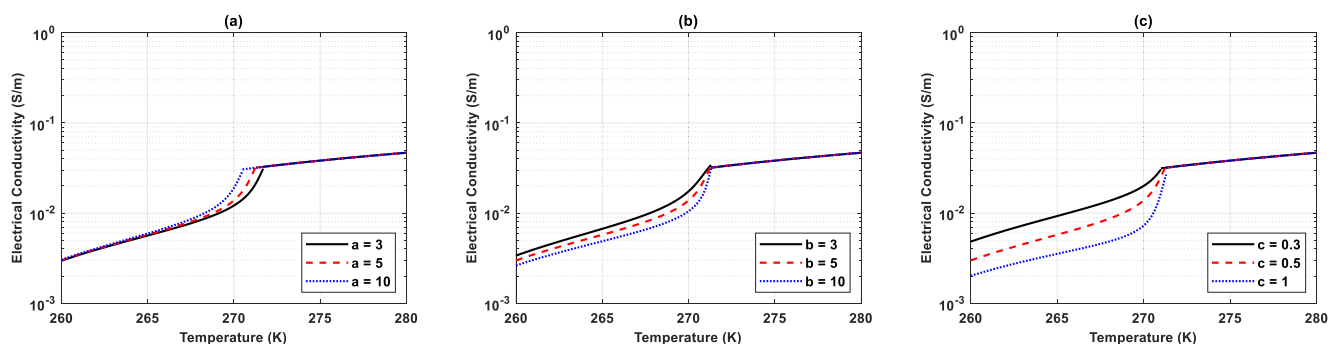


Figure 14. Conductivity dependence on the physical parameters of soil freezing characteristic curve model in partially saturated frozen porous media. (a) The influence of a on unsaturated electrical conductivity ($b = 5$ and $c = 0.5$); (b) the influence of b on unsaturated electrical conductivity ($a = 5$ and $c = 0.5$); (c) the influence of c on unsaturated electrical conductivity ($a = 5$ and $b = 5$). All other physical parameters of the proposed model remain constant with $\phi = 0.368$, $S_{w,0} = 0.800$, $C_0 = 0.1$ mol/L, $r_{\max} = 1 \times 10^{-5}$ m, $\alpha = 0.01$, $D_f = 1.200$, and $D_e = 1.350$.

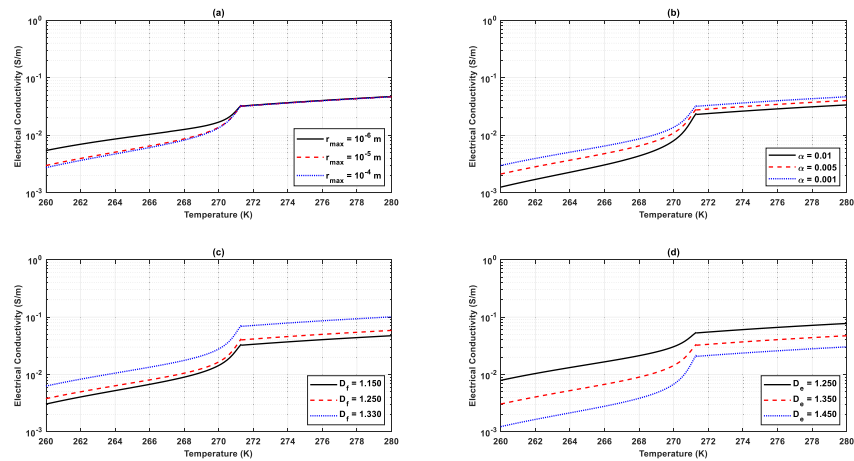


Figure 15. Conductivity dependence on geometric parameters related to pore size and pore tortuosity in partially saturated frozen porous media. (a) The effect of the maximum pore radius (r_{\max}) on unsaturated electrical conductivity ($\alpha = 0.01$, $D_f = 1.200$, and $D_e = 1.350$); (b) The effect of the ratio of the minimum pore radius to maximum pore radius (α) on unsaturated electrical conductivity ($r_{\max} = 1 \times 10^{-5}$ m, $D_f = 1.200$, and $D_e = 1.350$); (c) The effect of the fractal dimension of pore size (D_f) on unsaturated electrical conductivity ($r_{\max} = 1 \times 10^{-5}$ m, $\alpha = 0.01$, and $D_e = 1.350$); (d) The effect of the fractal dimension of pore tortuosity (D_e) on unsaturated electrical conductivity ($r_{\max} = 1 \times 10^{-5}$ m, $\alpha = 0.01$, and $D_f = 1.200$). All other physical parameters of the proposed model remain constant with $\phi = 0.368$, $S_{w,0} = 0.800$, $C_0 = 0.1$ mol/L, $a = 5$, $b = 5$, and $c = 0.5$.

study, the modeling parameters are given as: $r_{\max} = 1 \times 10^{-4}$ m, $\alpha = 0.01$, $D_f = 1.170$, and $D_e = 1.430$. For red clay, the modeling parameters with various initial water saturation and salinity are identified as: $r_{\max} = 3 \times 10^{-6}$ m, $\alpha = 0.001$, $D_f = 1.300$, and $D_e = 1.310$. Finally, for clayey silt, the four geometrical parameters are fitted as follows: $r_{\max} = 5 \times 10^{-6}$ m, $\alpha = 0.01$, $D_f = 1.230$, and $D_e = 1.330$. Meanwhile, the maximum pore radius (r_{\max}) and the ratio of the minimum pore radius to the maximum pore radius (α) can be measured through the PSD curve. The pore size distributions of three similar soil types (silty soil, quartz sand, and red clay) could be determined by the NMR method (Kou, 2020; Minagawa et al., 2008; Teng et al., 2020). The analysis indicates that the fitting parameters (r_{\max} and α) in the proposed model are consistent with the experimental values in the literature, thereby confirming the validity of the fitting values in this study. Moreover, fractal patterns can describe flow and transport properties for various soil types, including size distribution of pores and pore irregularities (e.g., tortuosity and constrictivity). It is noteworthy that the predicted values for the fractal dimension of pore size in this study are consistent with reference values found in the literature for different porous materials (Chen et al., 2020 for quartz sand; Chen et al., 2023 for clay; Giménez et al., 1997 for clayey silt). In summary, these published examples show that the proposed fractal-based model can reflect the dependence of the electrical conductivity on water saturation and salinity over a wide range of temperature, demonstrating the reasonableness of the modeling parameters.

In this study, we analyze the behavior of the proposed temperature-dependent model to predict the electrical conductivity and compare the predicted values with laboratory observations over wide ranges of temperature, initial water saturation and salinity. Several interesting aspects are worth further discussing here. First, the freezing temperature of red clay or clayey silt is lower than that of quartz sand for identical initial conditions. The freezing temperature decreases as the ionic concentration increases or the initial water saturation decreases. From the perspective of modeling parameters, the SFCC modeling parameter (a) controls the freezing point of the electrical conductivity-temperature curve. For red clay or clayey silt, this parameter is larger than for quartz sand, as shown in Table S3 in Supporting Information S1, leading to their lower freezing temperatures. Moreover, as indicated in Tables S5 and S6 in Supporting Information S1, the SFCC modeling parameter (a) increases with a decrease in initial water saturation or an increase in initial salinity, which reduces the freezing temperature of the electrical conductivity-temperature curve. In fact, this phenomenon can also be explained by the Young-Laplace effect and the Gibbs-Thomson effect (Equations 4 and 5). With a decrease in initial water saturation, liquid water retracts into extremely small capillaries. According to the Gibbs-Thomson effect, this results in a lower freezing temperature in unsaturated frozen porous medium. In addition, varying salt concentration changes the chemical potential of complex systems, thereby affecting the freezing point of the liquid water.

Additionally, red clay or clayey silt exhibit significantly higher electrical conductivity compared to quartz sand, and the increase in initial water saturation or initial salinity results in higher electrical conductivity over the entire temperature range. When exposed to positive temperature conditions, differences in the electrical conductivity for varying soil samples can be attributed to the effects of their size distribution of pores and pore irregularities (e.g., tortuosity and constrictivity). In this study, the smaller PSD and pore tortuosity of red clay and clayey silt compared to quartz sand, that is, the D_f of red clay or clayey silt is larger than that of quartz sand, while the α and D_e are smaller than that of quartz sand, result in a higher electrical conductivity between them above the freezing temperature. Moreover, ionic mobilities decrease as temperature declines, and the bulk electrical conduction diminishes when water saturation, salinity, and temperature decrease. Consequently, these factors result in a decline in electrical conductivity. As the temperature decreases below the freezing point, the capillary water freezes rapidly, especially in the larger pores, such as quartz sand. However, red clay or clayey silt, characterized by lower pore size distributions and larger specific surface areas, exhibits a significantly higher unfrozen water saturation at sub-zero temperatures, thereby resulting in higher electrical conductivity compared to quartz sand. For varying initial water saturation or salinity conditions, freezing leads to the variations in unfrozen water saturation and salt concentration. Therefore, the electrical conductivity of unsaturated frozen porous medium is primarily influenced by the unfrozen water saturation and ionic concentration. Four geometric parameters related to pore size (r_{\max} , α , and D_f) as well as pore tortuosity (D_e) remains stable over the entire water saturation and salinity ranges, which means that these parameters are mainly affected by the size distribution of pores and pore irregularities.

In reality, the electrolytic conduction could exist in all three pore-scale scenarios, not only the water-filled case. For instance, Li et al. (2015) explored the electrical conductance of two types of capillaries, considering the electrolytic conduction in both water-filled and non-wetting fluid-filled (thin residual water film) capillaries. However, given the extremely small and challenging-to-determine water film thickness at the solid ice-water interface in this study, our assumption is limited to surface conduction through the water film, thereby excluding electrolyte conduction. Similarly, the SFCC model proposed in Equation S2 in Supporting Information S1 only takes into account the capillary effect, neglecting the influence of the adsorption component. To minimize errors in surface electrical conduction, we adopted an empirical model from Wang et al. (2017), incorporating surface electrolyte conduction into bulk conduction.

6. Conclusion

Electrical and electromagnetic techniques allow for the non-intrusive characterization of water content in the subsurface, which makes them promising tools to study the hydro-thermal-mechanical processes in situ and follow the mechanisms of thaw-weakening and frost-heave damages in cold regions. Electrical conductivity is an important parameter that allows us to create physically-based relationships between electrical conductivity and temperature. It is indeed a very useful tool for problems at freezing temperatures. In this work, we propose a new physically-based model to describe the evolution of electrical conductivity as a function of temperature, initial water saturation and salinity. Then, we validated the proposed model against published data from the literature and new experimental data acquired in this study. The main conclusions of this work are as follows.

1. We assume that soil pores are composed of a bundle of tortuous capillaries whose pore size and tortuous length obey fractal distributions (D_f and D_e). Considering the Young-Laplace and Gibbs-Thomson effects, the total conductance is determined by the sum of the conductances of the three types of capillaries (that are occupied by water, ice and air) at pore scale. Based on the surface complexation model in the mineral-water, bulk ice-water and air-water interfaces, the proposed model at REV scale can be computed by using an upscaling procedure for predicting the electrical conductivity of the unsaturated frozen porous medium over a wide temperature, moisture and salinity ranges.
2. We evaluate the accuracy of the proposed model for the unsaturated porous media above the freezing temperature and for the frozen porous media under fully saturated conditions according to published data from the literature, illustrating that it is highly consistent with published experimental data. Meanwhile, the performance of the proposed model was evaluated using the new experimental data of electrical conductivity and unfrozen water saturation acquired in this study for different initial water saturations and salinities, indicating that it is also largely in agreement with the experimental data. The proposed model can predict the electrical conductivity of the porous medium over the entire temperature, water saturation and salinity ranges.

3. The freezing temperature of red clay or clayey silt is lower than that of quartz sand for identical initial conditions. As the ionic concentration increases or the initial water saturation decreases, the freezing temperature decreases. Additionally, red clay or clayey silt exhibits significantly higher electrical conductivity compared to quartz sand, and the increase in initial water saturation or initial salinity results in higher electrical conductivity over the entire temperature range. Furthermore, we observe that three SFCC modeling parameters are not only related to the pore volumetric contents of the pore, but also related to the initial conditions of the porous media (i.e., water saturation and salinity). However, four geometrical parameters related to pore size (r_{\max} , α , and D_p) as well as pore tortuosity (D_e) remains stable over the entire water saturation and salinity ranges, which means that these parameters are mainly affected by the size distribution of pores and pore irregularities.
4. The true and apparent formation factors can be determined by the proposed electrical conductivity model. In this study, we compare the evolution of the apparent formation factor as a function of porosity and as a function of water saturation. It was observed that the proposed model correctly reproduces the tendencies of the experimental data. It is worth noting that the true formation factor is unrelated to water saturation, whereas the apparent formation factor decreases as water saturation increases. Besides, we also compare the dependence of the apparent formation factor in the unsaturated frozen porous medium on temperature. The predicted results from the proposed model are largely in agreement with the experimental data.

The proposed capillary bundle model involves four fitting parameters (r_{\max} , α , D_p , and D_e), each with its own physical meaning. The maximum radius and the ratio of the minimum radius to the maximum radius can be determined from analyzing the PSD of the samples using the NMR method or mercury intrusion porosimetry. In this study, to reduce the number of parameters in the surface complexation model, we adopted the same equilibrium constant values and the total surface site density for different types of minerals (i.e., quartz sand, red clay, and clayey salt). However, to account for the significant differences in the specific surface conductivity among different mineral surfaces (e.g., montmorillonite, kaolinite, and illite), we will need to extend the proposed model in future research. Furthermore, in actual media, particularly in complex porous media like soils, sediments, and rocks, the pore structure can be significantly intricate, involving interconnections between pores. As a result, we will need to consider the effects of these interconnected pores, such as crossed cylindrical pores. Moreover, because the linear additive model of pore water conductivity is primarily efficient at low salinities, its application may result in an overestimation of pore water conductivity across various salinity levels. Given the absence of an appropriate physically-based model for negative temperatures at high concentrations, this opens up a new avenue for exploring enhancements in our future research.

Electrical conductivity measurements are highly valuable in permafrost research, as they can help estimate physical properties of frozen porous media such as temperature, liquid water content, and salinity. The proposed model and corresponding fitting parameters provide strong support for these measurements, particularly when investigating interactions among different physical properties. Electrical conductivity measurements offer crucial information, contributing to a more comprehensive understanding of subsurface permafrost characteristics. However, in real-field data, it is often necessary to distinguish their effects by combining other alternative monitoring methods (e.g., induced polarization and dielectric measurements) or physical parameters (e.g., complex conductivity and dielectric permittivity), since these electrophysical parameters change significantly when the water freezes (Duvillard et al., 2018; Léger et al., 2023).

Appendix A: Electrical Double-Layer Model of Mineral-Water Interface

We consider that mineral grains are in contact with a simple binary symmetric 1:1 electrolyte (e.g., NaCl) and that the pH is in the range 6–8. We obtain the distribution of the counterions and coions of EDL at the mineral-water interface (e.g., Leroy et al., 2008; Revil & Glover, 1997). In this work, as our experimental measurements of the electrical conductivity are made in the case of neutral pH (6–8), we neglect the effect of the relative equilibrium constants for the second protonation at the mineral-water interface, but the second protonation reaction should be considered in an acid environment. Additional assumption is that the zeta potential of mineral-water interface is equal to the electrical potential at the shear plane (d -plane in Figure 1e).

The electrochemical double-layer in the mineral-water interface consists of a Stern layer with strongly bounded ions (including inner and outer sphere surface complexes) and a diffuse layer with mobile ions (Figure 1e). The counterions of the outer sphere surface complexes in the Stern layer keep a certain mobility as in the diffuse layer. With this “dynamic Stern layer assumption”, the specific surface conductance at the mineral surface is composed

of two contributions: from the excess counterions contained in the outer sphere surface complexes of the Stern layer and from the diffuse layer. Therefore, the surface charge density Q_{s0} (in C/m^2) at the mineral surface, the surface charge density $Q_{s\beta}$ (in C/m^2) at the Stern layer, and the equivalent surface charge density Q_{ss} (in C/m^2) related to the excess of charge at the diffuse layer can be computed according to respectively:

$$Q_{s0} = -\frac{e_0\Gamma_s^0}{\alpha_s} \left[K_{s2} C_{Na^+}^f \exp\left(-\frac{e_0\varphi_{s\beta}}{k_b T}\right) + 1 \right], \quad (A1)$$

$$Q_{s\beta} = \frac{e_0\Gamma_s^0}{\alpha_s} K_{s2} C_{Na^+}^f \exp\left(-\frac{e_0\varphi_{s\beta}}{k_b T}\right), \quad (A2)$$

$$Q_{ss} = -\sqrt{8\varepsilon_f k_b T C_f} \sinh\left(\frac{e_0\varphi_{sd}}{2k_b T}\right), \quad (A3)$$

with

$$\alpha_s = 1 + K_{s1} C_{H^+}^f \exp\left(-\frac{e_0\varphi_{s0}}{k_b T}\right) + K_{s2} C_{Na^+}^f \exp\left(-\frac{e_0\varphi_{s\beta}}{k_b T}\right), \quad (A4)$$

where Γ_s^0 is the total surface site density of the mineral grain (in sites nm^{-2}), K_{s1} , K_{s2} are the intrinsic equilibrium constants of different types of amphoteric reactions in the mineral-water interface (values are shown in Table S1 in Supporting Information S1). In this study, we do not take into account the influence of different mineral surfaces on the specific surface conductance, thus we take the same equilibrium constant at the mineral-water interface for any type of materials (red clay, quartz sand and clayey silt) to compute the electrochemical properties (surface charge density, zeta potential and specific surface conductance) of the mineral surface in order to decrease the number of parameters when modeling the electrokinetic properties. The symbols $C_{H^+}^f$, $C_{Na^+}^f$ and C_f (in mol/L) represent the concentrations of the protons, the counterions (Na^+ in the free electrolyte) and the salinity in the free electrolyte, $C_{Na^+}^f = C_f$ and $C_{H^+}^f = 10^{-pH}$, ε_f is the pore water permittivity ($\varepsilon_f = 81\varepsilon_0$, $\varepsilon_0 \sim 8.85 \times 10^{-12}$ F m^{-1}), e_0 represents the elementary charge (taken positive, $e_0 = 1.6 \times 10^{-19}$ C), k_b is the Boltzmann constant (1.381×10^{-23} J K^{-1}), φ_{s0} , $\varphi_{s\beta}$, and φ_{sd} (in V) are the electrical potential at the mineral surface (0-plane), at the β - and d -planes, respectively. The electrical potentials are related by the series capacitor at the 0-, β - and d -planes. This yields

$$\varphi_{s0} - \varphi_{s\beta} = \frac{Q_{s0}}{C_{s1}}, \quad (A5)$$

and

$$\varphi_{s\beta} - \varphi_{sd} = -\frac{Q_{ss}}{C_{s2}}, \quad (A6)$$

where C_{s1} and C_{s2} are the (constant) integral capacities of the inner and outer parts of the Stern layer in the mineral-water interface, respectively, and the values of these capacities are listed in Table S1 in Supporting Information S1 (Leroy et al., 2008).

The global electroneutrality equation for EDL in the mineral grain and water interface is

$$Q_{s0} + Q_{s\beta} + Q_{ss} = 0. \quad (A7)$$

On the basis of the total surface site density (Γ_s^0) of the mineral surface, and of the associated equilibrium constants for surface reactions of mineral surface given by Leroy et al. (2008), we can determine the surface charge density and electrical potential at mineral surface, Stern layer and diffuse layer for different ionic concentrations based on Equations A1 to A7.

Since the major contribution of the specific surface conductance at the mineral-water interface is in the diffuse layer of mobile ions and in the Stern layer of bound counterions, the specific surface conductance Σ_{sw} (in S) is then computed using the following equation, relating to the surface charge density and to the temperature (Revil, 2012):

$$\Sigma_{sw} \approx (\beta_{0_Na}^{ref} Q_{s\beta} + \beta_{s_Na}^{ref} Q_{ss}) [1 + \alpha_T (T - T_{ref})], \quad (A8)$$

where $\beta_{0_Na}^{ref}$ and $\beta_{s_Na}^{ref}$ ($= \beta_{Na}^{ref}$) are the effective reference mobilities of the counterions in the Stern layer and in the diffuse layer at the reference temperature ($T_{ref} = 298$ K), respectively (in $m^2 s^{-1} V^{-1}$, values are shown in Table S1 in Supporting Information S1) (S. Li et al., 2016).

Appendix B: Electrical Double-Layer Model of Bulk Ice-Water Interface

Water molecules are organized in a tetrahedral lattice where hydrogen bonds provide the majority of the lattice energy in hexagonal ice Ih (hexagonal ice crystal). The arrangement of atoms of the ice lattice takes two different forms: one where the two hydrogen atoms bond covalently every oxygen atom and the other where one hydrogen atom is contained in every O-O vertex. Daigle (2021) and Kallay et al. (2003) considered the development of the surface chemical reactions for two types of surface sites (1 pK or 2 pK), and the distribution of charge within the electrical double-layer in the bulk ice-water interface in a manner analogous to existing modes for metal oxides in aqueous solutions.

In this study, we consider these two types of surface sites that exhibit vastly different behavior (very different pK) and compute their electrochemical properties in EDL of the interface between the bulk ice and liquid water. We consider that the electrolyte surrounding the ice is NaCl, and we ignore the adsorption and transport of chloride ions at bulk ice-water interface during the surface reaction, as well as that pH is in the range of 6–8. Due to the counterions in the Stern layer are prevented from penetrating into the bulk ice surface at the bulk ice-water interface, the Stern layer is assumed to be immediately adjacent to the bulk ice surface. We also ignore the influence of the second protonation and the corresponding equilibrium constant for the bulk ice-water interface. We consider four types of reactions: deprotonation of surface hydroxyls, ion association reaction on deprotonated sites (e.g., the adsorption of sodium cations), sorption of the protons, and adsorption of sodium cations on dangling O atoms. Therefore, the surface charge density Q_{i0} at the surface of the bulk ice (0-plane) as well as the equivalent surface charge density Q_{is} at the diffuse layer can be determined according to respectively

$$Q_{i0} = -\frac{e_0 \Gamma_i^0}{\alpha_i} \left[\left(K_{i1} + \frac{1}{K_{i3}} \right) \frac{1}{C_{H^+}^f} \exp\left(\frac{e_0 \varphi_{i0}}{k_b T}\right) \right], \quad (B1)$$

$$Q_{is} = -\sqrt{8 \epsilon_f k_b T C_f} \sinh\left(\frac{e_0 \varphi_{id}}{2 k_b T}\right), \quad (B2)$$

with

$$\alpha_i = 1 + \left(K_{i1} + \frac{1}{K_{i3}} \right) \frac{1}{C_{H^+}^f} \exp\left(\frac{e_0 \varphi_{i0}}{k_b T}\right) + \frac{K_{i2} C_{Na^+}^f}{K_{i3} C_{H^+}^f} \exp\left[\frac{e_0 (\varphi_{i0} - \varphi_{id})}{k_b T}\right], \quad (B3)$$

where Γ_i^0 (in sites nm^{-2}) represents the total surface site density of the bulk ice surface, K_{i1} , K_{i2} and K_{i3} are the intrinsic equilibrium constants of different types of amphoteric reactions in the bulk ice-water interface are listed in Table S1 in Supporting Information S1; φ_{i0} and φ_{id} (in V) are the electrical potential at the 0-plane (bulk ice surface) and at the d -plane (zeta potential), respectively. The electrical potentials are associated by the series capacitor at the 0-plane and d -plane. This yields

$$\varphi_{i0} - \varphi_{id} = \frac{Q_{i0}}{C_i}, \quad (B4)$$

where C_i is the (constant) integral capacity of the Stern layer in the interface between bulk ice and liquid water film, and $C_i = 1 \text{ F m}^{-2}$ from Daigle (2021).

The electroneutrality condition for EDL in the bulk ice-water interface is given by

$$Q_{i0} + Q_{is} = 0. \quad (\text{B5})$$

With the total surface site density (Γ_i^0) of bulk ice surface, and the associated equilibrium constants for surface reactions of bulk ice-water interface (Daigle, 2021; Kallay et al., 2003), we can determine the surface charge density and the electrical potential at the bulk ice surface and the diffuse layer for different salinities based on Equations B1 to B5.

We consider that the mobile ions in the diffuse layer affect the specific surface conductance in the electrical double-layer at the bulk ice-water interface. Therefore, we can determine the specific surface conductance Σ_{iw} (in S) as a function of surface charge density (Revil, 2012):

$$\Sigma_{iw} \approx \beta_{s_Na}^{\text{ref}} Q_{is} [1 + \alpha_T (T - T_{\text{ref}})]. \quad (\text{B6})$$

Appendix C: Electrical Double-Layer Model of Air-Water Interface

Leroy et al. (2012) developed a unified surface complexation model that describes the electrochemical properties of the gas/water interface at a low ionic concentration, which is similar to the traditional “one site/two pK ” model (Davis et al., 1978). We hence consider the air-water film interface in contact with a 1:1 aqueous electrolyte such as NaCl and the pH of fluid is assume to equal 6–8. Since the available experimental measurements of the electrical conductivity are of neutral pH (6–8), we only consider the chemical reaction linked with the surface adsorption of protons and chloride (because the chloride anion is closer to the surface than the sodium cation at high ionic strengths). According to the surface complexation model of the air-water film interface derived by Leroy et al. (2012), the surface charge density Q_{a0} at the surface of air (the sum of the surface site densities of charged surface groups), and the equivalent surface charge density Q_{as} at the diffuse layer can be determined as follows respectively

$$Q_{a0} = -\frac{e_0 \Gamma_a^0}{\alpha_a} [K_{a1} K_{a2} C_{\text{H}^+}^f C_{\text{Cl}^-}^f + 1], \quad (\text{C1})$$

$$Q_{as} = -\sqrt{8\epsilon_f k_b T C_f} \sinh\left(\frac{e_0 \varphi_{ad}}{2k_b T}\right), \quad (\text{C2})$$

with

$$\alpha_a = 1 + K_{a1} C_{\text{H}^+}^f \exp\left(-\frac{e_0 \varphi_{a0}}{k_b T}\right) + K_{a1} K_{a2} C_{\text{H}^+}^f C_{\text{Cl}^-}^f, \quad (\text{C3})$$

where Γ_a^0 (in sites nm^{-2}) is the total surface site density of the air-water interface, K_{a1} , and K_{a2} are the associated equilibrium constants for the different reactions of the air-water interface, their values are shown in Table S1 in Supporting Information S1; the symbol $C_{\text{Cl}^-}^f$ (in mol/L) represents the salinity of the chloride electrolyte in the free electrolyte, $C_{\text{Cl}^-}^f = C_f \varphi_{a0}$ and φ_{ad} are, respectively, the electrical potential at the 0-plane and at the d -plane (in V). The electrical potentials are given by

$$\varphi_{a0} - \varphi_{ad} = \frac{Q_{a0}}{C_a}, \quad (\text{C4})$$

where C_a is the (constant) integral capacity of the Stern layer in the air-water interface, and $C_a = 0.0258 \text{ F m}^{-2}$ obtained by Leroy et al. (2012).

The global electroneutrality condition for the electrical double-layer at the air-water interface implies the following:

$$Q_{a0} + Q_{as} = 0. \quad (C5)$$

On the basis of the total surface site density (Γ_a^0) of air surface, the associated equilibrium constants for surface reactions of air-water interface are given by Leroy et al. (2012). Then we can determine the surface charge density and electrical potential at the bulk ice surface and the diffuse layer for different concentrations based on Equations C1 to C5.

Leroy et al. (2012) developed a specific surface conductance model including the contribution of proton electro-migration at the 0-plane in the Stern layer (the effect of the sorption of the protons) and the contribution of the counterions electro-migration in the diffuse layer. Considering a relatively neutral pH environment, thus we only consider the influence of the counterions electro-migration in the diffuse layer on the surface conductivity at the air-water interface. Therefore, we can determine the relationship between specific surface conductance Σ_{aw} (in S) and surface charge density in the diffuse layer:

$$\Sigma_{aw} \approx \beta_{s_Na}^{eff} Q_{as} [1 + \alpha_T (T - T_{ref})]. \quad (C6)$$

Appendix D: Apparent Formation Factor

The formation factor (F) is a strictly geometrical parameter that can be used to describe the geometry of the pore space (e.g., Archie, 1942; Coperey, Revil, Abdulsamad, et al., 2019; Revil, Coperey, et al., 2018; Revil et al., 2014; Revil, Soueid Ahmed, & Matthai, 2018). In absence of surface conductivity and when the pore space is occupied only by liquid water (i.e., no ice, no air), the formation factor can be defined as the ratio of the actual pore water conductivity to the electrical conductivity of the porous medium. From Equation 20, we can obtain the formation factor as a function of the porosity:

$$F = \frac{\left(\tau_g^{eff}\right)^2 (D_e - D_f + 1) [1 - \alpha^{3-D_e-D_f}]}{\phi (3 - D_e - D_f) \{1 - \alpha^{D_e-D_f+1}\}}. \quad (D1)$$

In the following, we also define an apparent formation factor (F_a) that depends on the water saturation and the unfrozen water content. The use of the apparent formation factor is frequent in the literature to highlight the effect of the water saturation (e.g., Mainault et al., 2018) or unfrozen water content (e.g., Coperey, Revil, Abdulsamad, et al., 2019). Following our model description, the apparent formation factor under partial water saturation above the freezing temperature is obtained as

$$F_a(S_{w,0}) = \frac{\left(\tau_g^{eff}\right)^2 (D_e - D_f + 1) [1 - \alpha^{3-D_e-D_f}]}{\phi (3 - D_e - D_f) \left\{ \left[\alpha^{3-D_e-D_f} + S_{w,0} (1 - \alpha^{3-D_e-D_f}) \right]^{\frac{D_e-D_f+1}{3-D_e-D_f}} - \alpha^{D_e-D_f+1} \right\}}. \quad (D2)$$

And the apparent formation factor as a function of the unfrozen water saturation at freezing temperature is given by

$$F_a(S_u) = \frac{\left(\tau_g^{eff}\right)^2 (D_e - D_f + 1) [1 - \alpha^{3-D_e-D_f}]}{\phi (3 - D_e - D_f) \left\{ \left[\alpha^{3-D_e-D_f} + S_u (1 - \alpha^{3-D_e-D_f}) \right]^{\frac{D_e-D_f+1}{3-D_e-D_f}} - \alpha^{D_e-D_f+1} \right\}}. \quad (D3)$$

Equation D1 illustrates that the formation factor above the freezing temperature is linked with the geometrical tortuosity (τ_g^{eff}) and the microstructural parameters of the REV (D_e , D_f , ϕ , α), but is independent of the water saturation, and it is inversely proportional to the porosity in a similar form as reported in Thanh et al. (2019, 2020).

However, the apparent formation factor is related not only to the microstructural parameters of the porous medium, but also to the water saturation ($S_{w,0}$) or to the unfrozen water saturation (S_u) from Equations D2 and D3.

Notations

T	Temperature of the REV (K)
T_0	Freezing temperature of bulk water (K)
T_m	Freezing temperature of the porous medium (K)
T_{ref}	Reference temperature (K)
T_s	Liquid water surface tension (N m^{-1})
r	Radius of the capillary tube (m)
r_1	Radius of the capillary tube filled with liquid water (m)
r_2	Radius of the capillary tube occupied by bulk ice (m)
r_3	Radius of the capillary tube occupied by air (m)
r_i	Critical freezing radius (either filled with liquid water or bulk ice) of the REV (m)
r_h	Critical freezing radius (either occupied by bulk ice or air) of the REV (m)
r_{\max}	Maximum radius of the capillary tube (m)
r_{\min}	Minimum radius of the capillary tube (m)
g	Acceleration of gravity (m s^{-2})
α	Ratio of the minimum pore radius to the maximum pore radius (–)
β	Air-water-solid contact angle (–)
σ_{sl}	Ice-water interfacial free energy (J m^{-2})
σ_w	Electrical conductivity of pore water (S/m)
σ	Electrical conductivity of the porous medium (S/m)
L	Length of the sample (m)
L_f	Latent heat of phase transformation (J/kg)
L_e	Length of the capillary (tortuous length) (m)
L_0	REV length (m)
ρ_i	Density of ice (kg m^{-3})
ρ_w	Liquid water volume density (kg m^{-3})
ρ_g	Grain density (kg m^{-3})
R	Resistance value of experiments (Ω)
$R(r)$	Total resistance of the three types of capillary (Ω)
R_1	Resistance of the capillary filled with liquid water ($r_{\min} < r < r_i$) (Ω)
R_2	Resistance of the capillary occupied by bulk ice ($r_i < r < r_h$) (Ω)
R_3	Resistance of the capillary occupied by air ($r_h < r < r_{\max}$) (Ω)
R_0	Resistance of the porous media at REV scale (Ω)
Σ_{aw}	Specific surface conductance at the air-water surface (S)

Σ_{sw}	Specific surface conductance at the mineral-water surface (S)
Σ_{iw}	Specific surface conductance at the bulk ice-water surface (S)
$\Sigma(r_1, r_2, r_3)$	Total conductance of the three capillaries (they are occupied by water, ice and air) (S)
A_{REV}	Cross-section area of REV (m ²)
$f(r)$	Capillary tube distribution function of the REV (–)
F	Formation factor of the porous medium (–)
$F_a(S_{w,0})$	Apparent formation factor above the freezing temperature (–)
$F_a(S_u)$	Apparent formation factor below the freezing temperature (–)
S	Area of the sample (m ²)
n	Unfrozen exponent (–)
$N(\geq r)$	Number of the capillaries (with radius larger than r) (–)
N_A	Avogadro's number (mol ^{–1})
ϕ	Porosity of the REV (–)
τ_g^{eff}	Effective geometrical tortuosity of the porous medium (–)
$S_{w,0}$	Initial water saturation of the REV (–)
S_u	Unfrozen water saturation of the REV (–)
h_m	Initial pressure head (m)
D_f	Fractal dimension for pore space (–)
D_e	Fractal dimension of capillary tortuosity (–)
a	Physical parameters of the SFCC (–)
b	Physical parameters of the SFCC (–)
c	Physical parameters of the SFCC (–)
CEC	Cation exchange capacity (C/kg)
e_0	Elementary charge (C)
k_b	Boltzmann's constant (J K ^{–1})
ϵ_f	Permittivity of the pore water (F m ^{–1})
C_0	Initial ionic concentration of the REV (mol/L)
C_u	Ionic concentration of the REV in frost state (mol/L)
C_f	Salinity in the free electrolyte (mol/L)
$C_{H^+}^f$	Ionic concentration of the protons in the free electrolyte (mol/L)
$C_{Na^+}^f$	Ionic concentration of sodium cations in the free electrolyte (mol/L)
C_i^f	Concentration of ionic species i in the free electrolyte (mol/L)
$C_{Cl^-}^f$	Concentration of chloride in the free electrolyte (mol/L)
q_i	Charge of species i in the free electrolyte (C)
$B(T)$	Apparent mobility of the counterions for surface conduction (m ² s ^{–1} V ^{–1})
$\lambda(T)$	Apparent mobility of the counterions for the polarization (m ² s ^{–1} V ^{–1})

β_i	Mobility of ionic species i in the free electrolyte ($\text{m}^2 \text{s}^{-1} \text{V}^{-1}$)
β_i^{ref}	Reference mobility of ionic species i in the free electrolyte ($\text{m}^2 \text{s}^{-1} \text{V}^{-1}$)
$\beta_{\text{Na}}^{\text{ref}}$	Reference mobility of ionic species Na^+ in the free electrolyte ($\text{m}^2 \text{s}^{-1} \text{V}^{-1}$)
$\beta_{0\text{-Na}}^{\text{ref}}$	Effective reference mobility of counterions in the Stern layer ($\text{m}^2 \text{s}^{-1} \text{V}^{-1}$)
$\beta_{s\text{-Na}}^{\text{ref}}$	Effective reference mobility of counterions in the diffuse layer ($\text{m}^2 \text{s}^{-1} \text{V}^{-1}$)
$\beta_{\text{Cl}}^{\text{ref}}$	Reference mobility of ionic species Cl^- in the free electrolyte ($\text{m}^2 \text{s}^{-1} \text{V}^{-1}$)
$\beta_{\text{H}}^{\text{ref}}$	Reference mobility of ionic species H^+ in the free electrolyte ($\text{m}^2 \text{s}^{-1} \text{V}^{-1}$)
$\beta_{\text{OH}}^{\text{ref}}$	Reference mobility of ionic species OH^- in the free electrolyte ($\text{m}^2 \text{s}^{-1} \text{V}^{-1}$)
α_T	Temperature factor (K^{-1})
Γ_s^0	Total surface site density of the mineral surface (Sites nm^{-2})
Γ_i^0	Total surface site density of the ice surface (Sites nm^{-2})
Γ_a^0	Total surface site density of the air surface (Sites nm^{-2})
K_{s1}	Equilibrium constant of deprotonation at the mineral-water interface (–)
K_{s2}	Equilibrium constant of sodium adsorption at the mineral-water interface (–)
K_{i1}	Equilibrium constant for deprotonation at the ice-water interface (–)
K_{i2}	Equilibrium constant for sodium sorption at the ice-water interface (–)
K_{i3}	Equilibrium constant for H^+ sorption on dangling O at the ice-water interface (–)
K_{a1}	Equilibrium constant associated with surface adsorption of protons at ($>\text{X}^-$) sites at the air-water interface (–)
K_{a2}	Equilibrium constant associated with surface adsorption of chloride at ($>\text{XH}^+$) sites at the air-water interface (–)
K_g	Geometrical factor of the sample (m)
C_{s1}	Capacities of the inner parts of the Stern layer in the mineral-water interface (F m^{-2})
C_{s2}	Capacities of the outer parts of the Stern layer in the mineral-water interface (F m^{-2})
C_i	Capacity of the Stern layer at the bulk ice-water interface (F m^{-2})
C_a	Capacities of the Stern layer in the air-water interface (F m^{-2})
Q_{s0}	Surface charge density at the surface of the mineral (mineral-water interface) (C)
$Q_{s\beta}$	Surface charge density at the Stern layer (mineral-water interface) (C)
Q_{ss}	Surface charge density at the diffuse layer (mineral-water interface) (C)
φ_{s0}	Electrical potential at the mineral surface (mineral-water interface- 0-plane) (V)
$\varphi_{s\beta}$	Electrical potential at the β -plane (mineral-water interface) (V)
φ_{sd}	Electrical potential at the d -plane (mineral-water interface) (V)
Q_{i0}	Surface charge density at the surface of the bulk ice (bulk ice-water interface) (C)
Q_{is}	Surface charge density at the diffuse layer (bulk ice-water interface) (C)
φ_{i0}	Electrical potential at the mineral surface (bulk ice-water interface- 0-plane) (V)
φ_{id}	Electrical potential at the d -plane (bulk ice-water interface) (V)

Q_{a0}	Surface charge density at the surface of the air (air-water interface) (C)
Q_{as}	Surface charge density at the diffuse layer (air-water interface) (C)
φ_{a0}	Electrical potential at the 0-plane (air-water interface) (V)
φ_{ad}	Electrical potential at the d -plane (air-water interface) (V)

Data Availability Statement

The present study is supplemented by Supporting Information. The experimental data of frozen porous media for evaluating the evolution of electrical conductivity as a function of temperature are openly accessible in the Hydrogeophysics community via Zenodo under different initial water saturations and salinities: <https://doi.org/10.5281/zenodo.7688602>. Additionally, Matlab codes for calculating the predicted results of electrical conductivity are also available through this link.

References

- Amankwah, S. K., Ireson, A. M., Maulé, C., Brannen, R., & Mathias, A. (2021). A model for the soil freezing characteristic curve that represents the dominant role of salt exclusion. *Water Resources Research*, 57(8), e2021WR030070. <https://doi.org/10.1029/2021WR030070>
- Andersland, O. B., & Ladanyi, B. (2004). *Frozen ground engineering* (2nd). Wiley.
- Anderson, D. M. (1967). The interface between ice and silicate surfaces. *Journal of Colloid and Interface Science*, 25(2), 174–191. [https://doi.org/10.1016/0021-9797\(67\)90021-5](https://doi.org/10.1016/0021-9797(67)90021-5)
- Archie, G. E. (1942). The electrical resistivity log as an aid in determining some reservoir characteristics. *Transactions of the AIME*, 146(01), 54–62. <https://doi.org/10.2118/942054-G>
- Bai, R., Lai, Y., Zhang, M., & Gao, J. (2018). Water-vapor-heat behavior in a freezing unsaturated coarse-grained soil with a closed top. *Cold Regions Science and Technology*, 155, 120–126. <https://doi.org/10.1016/j.coldregions.2018.08.007>
- Banin, A., & Anderson, D. M. (1974). Effects of salt concentration changes during freezing on the unfrozen water content of porous materials. *Water Resources Research*, 10(1), 124–128. <https://doi.org/10.1029/WR10i001p00124>
- Binley, A., Cassiani, G., Middleton, R., & Winship, P. (2002). Vadose zone flow model parameterisation using cross-borehole radar and resistivity imaging. *Journal of Hydrology*, 267(3–4), 147–159. [https://doi.org/10.1016/S0022-1694\(02\)00146-4](https://doi.org/10.1016/S0022-1694(02)00146-4)
- Binley, A., Hubbard, S. S., Huisman, J. A., Revil, A., Robinson, D. A., Singha, K., & Slater, L. D. (2015). The emergence of hydrogeophysics for improved understanding of subsurface processes over multiple scales. *Water Resources Research*, 51(6), 3837–3866. <https://doi.org/10.1002/2015WR017016>
- Breede, K., Kemna, A., Esser, O., Zimmermann, E., Vereecken, H., & Huisman, J. (2011). Joint measurement setup for determining spectral induced polarization and soil hydraulic properties. *Vadose Zone Journal*, 10(2), 716–726. <https://doi.org/10.2136/vzj2010.0110>
- Bussière, L., Schmutz, M., Fortier, R., Lemieux, J. M., & Dupuy, A. (2022). Near-surface geophysical imaging of a thermokarst pond in the discontinuous permafrost zone in Nunavik (Québec), Canada. *Permafrost and Periglacial Processes*, 33(4), 353–369. <https://doi.org/10.1002/ppp.2166>
- Chen, H., Chen, K., Yang, M. H., & Xu, P. (2020). A fractal capillary model for multiphase flow in porous media with hysteresis effect. *International Journal of Multiphase Flow*, 125, 103208. <https://doi.org/10.1016/j.ijmultiphaseflow.2020.103208>
- Chen, K., Chen, W., & Liang, F. Y. (2023). Fractal-based hydraulic model of unsaturated flow in deformable soils considering the evolution of pore size distribution. *Journal of Hydrology*, 620, 129501. <https://doi.org/10.1016/j.jhydrol.2023.129501>
- Christensen, A. F., He, H., Dyck, M. F., Lenore Turner, E., Chanasyk, D. S., Naeth, M. A., & Nichol, C. (2013). In situ measurement of snowmelt infiltration under various topsoil cap thicknesses on a reclaimed site. *Canadian Journal of Soil Science*, 93(4), 497–510. <https://doi.org/10.4141/cjss2012-048>
- Clayton, W. S. (2017). In situ measurement of meltwater percolation flux in seasonal alpine snowpack using self-potential and capillary pressure sensors. *The Cryosphere Discussions*, 2017, 1–21. <https://doi.org/10.5194/tc-2017-187>
- Clayton, W. S. (2021). Measurement of unsaturated meltwater percolation flux in seasonal snowpack using self-potential. *Journal of Glaciology*, 68(267), 25–40. <https://doi.org/10.1017/jog.2021.67>
- Coperey, A., Revil, A., Abdulsamad, F., Stutz, B., Duvillard, P. A., & Ravel, L. (2019). Low-frequency induced polarization of porous media undergoing freezing: Preliminary observations and modeling. *Journal of Geophysical Research: Solid Earth*, 124(5), 4523–4544. <https://doi.org/10.1029/2018JB017015>
- Coperey, A., Revil, A., & Stutz, B. (2019). Electrical conductivity versus temperature in freezing conditions: A field experiment using a basket geothermal heat exchanger. *Geophysical Research Letters*, 46(24), 14531–14538. <https://doi.org/10.1029/2019GL084962>
- Dafflon, B., Hubbard, S., Ulrich, C., Peterson, J., Wu, Y. X., Wainwright, H., & Kneafsey, T. J. (2016). Geophysical estimation of shallow permafrost distribution and properties in an ice-wedge polygon-dominated Arctic tundra region. *Geophysics*, 81(1), WA247–WA263. <https://doi.org/10.1190/geo2015-0175.1>
- Daigle, H. (2021). Structure of the electrical double layer at the ice-water interface. *Journal of Chemical Physics*, 154(21), 214703. <https://doi.org/10.1063/5.0048817>
- Davis, J. A., James, R. O., & Leckie, J. O. (1978). Surface ionization and complexation at the oxide/water interface. *Journal of Colloid and Interface Science*, 63(3), 480–499. [https://doi.org/10.1016/S0021-9797\(78\)80009-5](https://doi.org/10.1016/S0021-9797(78)80009-5)
- Doussan, C., & Ruy, S. (2009). Prediction of unsaturated soil hydraulic conductivity with electrical conductivity. *Water Resources Research*, 45(10), W10408. <https://doi.org/10.1029/2008WR007309>
- Duvillard, P. A., Magnin, F., Revil, A., Legay, A., Ravel, L., Abdulsamad, F., & Coperey, A. (2021). Temperature distribution in a permafrost-affected rock ridge from conductivity and induced polarization tomography. *Geophysical Journal International*, 225(2), 1207–1221. <https://doi.org/10.1093/gji/ggaa597>

Acknowledgments

The authors strongly thank the Editor, the Associate Editor, and the two reviewers (Philippe Leroy and an anonymous one) for kind and constructive comments. Support for this work was provided by China Scholarship Council (CSC) project (Grant 202106370053). This research was also supported by the National Natural Science Foundation of China (No. 52178376), and the Natural Science Foundation of Hunan Province (2022JJ10076). Furthermore, we would like to express our gratitude to the School of civil engineering (CSU) for granting us access to the laboratory experimental apparatus for electrical resistance experiments (LCR setup) and for SFCC experiments (NMR method).

- Duvillard, P. A., Revil, A., Qi, Y., Soueid Ahmed, A., Coperey, A., & Ravanel, L. (2018). Three-dimensional electrical conductivity and induced polarization tomography of a rock glacier. *Journal of Geophysical Research: Solid Earth*, *123*(11), 9528–9554. <https://doi.org/10.1029/2018JB015965>
- Giménez, G., Perfect, E., Rawls, W. J., & Pachepsky, Y. (1997). Fractal models for predicting soil hydraulic properties: A review. *Engineering Geology*, *48*(3–4), 161–183. [https://doi.org/10.1016/S0013-7952\(97\)00038-0](https://doi.org/10.1016/S0013-7952(97)00038-0)
- Gleeson, T., Wang-Erlandsson, L., Porkka, M., Zipper, S. C., Jaramillo, F., Gerten, D., et al. (2020). Illuminating water cycle modifications and Earth system resilience in the Anthropocene. *Water Resources Research*, *56*(4), e2019WR024957. <https://doi.org/10.1029/2019WR024957>
- Guarracino, L., & Jougnot, D. (2018). A physically based analytical model to describe effective excess charge for streaming potential generation in water saturated porous media. *Journal of Geophysical Research: Solid Earth*, *123*(1), 52–65. <https://doi.org/10.1002/2017JB014873>
- Guarracino, L., Rötting, T., & Carrera, J. (2014). A fractal model to describe the evolution of multiphase flow properties during mineral dissolution. *Advances in Water Resources*, *67*, 78–86. <https://doi.org/10.1016/j.advwatres.2014.02.011>
- Haarder, E. B., Jensen, K. H., Binley, A., Nielsen, L., Uglebjerg, T. B., & Looms, M. C. (2015). Estimation of recharge from long-term monitoring of saline tracer transport using electrical resistivity tomography. *Vadose Zone Journal*, *14*(7), 1–13. <https://doi.org/10.2136/vzj2014.08.0110>
- Hauck, C., Botcher, M., & Maurer, H. (2011). A new model for estimating subsurface ice content based on combined electrical and seismic data sets. *The Cryosphere*, *5*(2), 453–468. <https://doi.org/10.5194/tc-5-453-2011>
- Hayashi, M., van der Kamp, G., & Schmidt, R. (2003). Focused infiltration of snowmelt water in partially frozen soil under small depressions. *Journal of Hydrology*, *270*(3–4), 214–229. [https://doi.org/10.1016/S0022-1694\(02\)00287-1](https://doi.org/10.1016/S0022-1694(02)00287-1)
- He, H. L., Dyck, M., Zhao, Y., Si, B. C., Jin, H. J., Zhang, T. J., et al. (2016). Evaluation of five composite dielectric mixing models for understanding relationships between effective permittivity and unfrozen water content. *Cold Regions Science and Technology*, *130*, 33–42. <https://doi.org/10.1016/j.coldregions.2016.07.006>
- Hermans, T., Goderniaux, P., Damien, J., Fleckenstein, J. H., Brunner, P., Nguyen, F., et al. (2023). Advancing measurements and representations of subsurface heterogeneity and dynamic processes: Towards 4D hydrogeology. *Hydrology and Earth System Sciences*, *27*(1), 255–287. <https://doi.org/10.5194/hess-27-255-2023>
- Herring, T., Cey, E., & Pidlisecky, A. (2019). Electrical resistivity of a partially saturated porous medium at subzero temperatures. *Vadose Zone Journal*, *18*, 1–11. <https://doi.org/10.2136/vzj2019.02.0019>
- Holloway, J., & Lewkowicz, A. (2019). Field and laboratory investigation of electrical resistivity-temperature relationships, Southern Northwest Territories. In *8th International conference on cold regions engineering and 8th Canadian permafrost conference* (pp. 64–72). <https://doi.org/10.1061/9780784482599.008>
- Hu, S. J., Zhang, C., & Lu, N. (2023). Quantifying coupling effects between soil matric potential and osmotic potential. *Water Resources Research*, *59*(2), e2022WR033779. <https://doi.org/10.1029/2022WR033779>
- IPCC. (2019). The ocean and cryosphere in a changing climate. IPCC special report on the ocean and cryosphere in a changing climate, 1155.
- Jin, X., Yang, W., Gao, X. Q., Zhao, J. Q., Li, Z. C., & Jiang, J. X. (2020). Modeling the unfrozen water content of frozen soil based on the absorption effects of clay surfaces. *Water Resources Research*, *56*(12), e2020WR027482. <https://doi.org/10.1029/2020WR027482>
- Jougnot, D., Ghorbani, A., Revil, A., Leroy, P., & Cosenza, P. (2010). Spectral induced polarization of partially saturated clay-rocks: A mechanistic approach. *Geophysical Journal International*, *180*(1), 210–224. <https://doi.org/10.1111/j.1365-246X.2009.04426.x>
- Jougnot, D., Linde, N., Haarder, E. B., & Looms, M. C. (2015). Monitoring of saline tracer movement with vertically distributed self-potential measurements at the HOBE agricultural test site, Voulund, Denmark. *Journal of Hydrology*, *521*, 314–327. <https://doi.org/10.1016/j.jhydrol.2014.11.041>
- Jurin, M. (1718). An account of some experiments shown before the Royal Society; with an enquiry into the cause of the ascent and suspension of water in capillary tubes. *Philosophical Transactions Royal Society*, *30*(355), 739–747. <https://doi.org/10.1098/rstl.1717.0026>
- Kallay, N., Čop, A., Chibowski, E., & Holysz, L. (2003). Reversible charging of the ice–water interface: II. Estimation of equilibrium parameters. *Journal of Colloid and Interface Science*, *259*(1), 89–96. [https://doi.org/10.1016/S0021-9797\(02\)00179-0](https://doi.org/10.1016/S0021-9797(02)00179-0)
- Kemna, A., Vanderborght, J., Kulesa, B., & Vereecken, H. (2002). Imaging and characterisation of subsurface solute transport using electrical resistivity tomography (ERT) and equivalent transport models. *Journal of Hydrology*, *267*(3–4), 125–146. [https://doi.org/10.1016/S0022-1694\(02\)00145-2](https://doi.org/10.1016/S0022-1694(02)00145-2)
- Kou, J. Y. (2020). Study on the influence of soil microstructure on the hydraulic properties of soil (PhD Thesis). Central South University. (In Chinese with English abstract).
- Kulesa, B., Chandler, D., Revil, A., & Essery, R. (2012). Theory and numerical modeling of electrical self-potential signatures of unsaturated flow in melting snow. *Water Resources Research*, *48*(9), W09511. <https://doi.org/10.1029/2012WR012048>
- Kulesa, B., Hubbard, B., & Brown, G. H. (2003). Cross-coupled flow modeling of coincident streaming and electrochemical potentials and application to subglacial self-potential data. *Journal of Geophysical Research*, *108*(B8), 2381. <https://doi.org/10.1029/2001JB001167>
- Lai, Z., Zhao, X., Tang, R., & Yang, J. (2021). Electrical conductivity-based estimation of unfrozen water content in saturated saline frozen sand. *Advances in Civil Engineering*, *2021*, e8881304. <https://doi.org/10.1155/2021/8881304>
- Lebeau, M., & Konrad, J. M. (2010). A new capillary and thin film flow model for predicting the hydraulic conductivity of unsaturated porous media. *Water Resources Research*, *46*(1), 1–15. <https://doi.org/10.1029/2010WR009092>
- Lebeau, M., & Konrad, J. M. (2012). An extension of the capillary and thin film flow model for predicting the hydraulic conductivity of air-free frozen porous media. *Water Resources Research*, *48*(7), W07523. <https://doi.org/10.1029/2012WR011916>
- Léger, E., Saintenoy, A., Serhir, M., Costard, F., & Grenier, C. (2023). Brief communication: Monitoring active layer dynamics using a light-weight nimble ground-penetrating radar system—a laboratory analogue test case. *The Cryosphere*, *17*(3), 1271–1277. <https://doi.org/10.5194/tc-17-1271-2023>
- Leroy, P., Jougnot, D., Revil, A., Lassin, A., & Azaroual, M. (2012). A double layer model of the gas bubble/water interface. *Journal of Colloid and Interface Science*, *388*(1), 243–256. <https://doi.org/10.1016/j.jcis.2012.07.029>
- Leroy, P., Revil, A., Kemna, A., Cosenza, P., & Ghorban, A. (2008). Complex conductivity of water-saturated packs of glass beads. *Journal of Colloid and Interface Science*, *321*(1), 103–117. <https://doi.org/10.1016/j.jcis.2007.12.031>
- Li, M., Tang, Y. B., Bernabé, Y., Zhao, J. Z., Li, X. F., Bai, X. Y., & Zhang, L. H. (2015). Pore connectivity, electrical conductivity, and partial water saturation: Network simulations. *Journal of Geophysical Research: Solid Earth*, *120*(6), 4055–4068. <https://doi.org/10.1002/2014JB011799>
- Li, S., Leroy, P., Heberling, F., Devau, N., Jougnot, D., & Chiaberge, C. (2016). Influence of surface conductivity on the apparent zeta potential of calcite. *Journal of Colloid and Interface Science*, *468*, 262–275. <https://doi.org/10.1016/j.jcis.2016.01.075>
- Loisel, J., Gallego-Sala, A. V., Amesbury, M. J., Magnan, G., Anshari, G., Beilman, D. W., et al. (2021). Expert assessment of future vulnerability of the global peatland carbon sink. *Nature Climate Change*, *11*(1), 70–77. <https://doi.org/10.1038/s41558-020-00944-0>

- Luo, H. L., Jougnot, D., Jost, A., Teng, J. D., & Thanh, L. D. (2023). A capillary bundle model for the electrical conductivity of saturated frozen porous media. *Journal of Geophysical Research: Solid Earth*, *128*(3), e2022JB025254. <https://doi.org/10.1029/2022JB025254>
- Luo, H. L., Teng, J. D., Zhang, S., & Sheng, D. C. (2021). Study on the relationship between unfrozen water content and electrical conductivity in frozen soils. *Chinese Journal of Rock Mechanical and Engineering*, *40*(5), 1068–1079. (in Chinese). Retrieved from <http://rockmech.whrsm.ac.cn/CN/Y2021/V40/I5/1068>
- Maineult, A., Jougnot, D., & Revil, A. (2018). Variations of petrophysical properties and spectral induced polarization in response to drainage and imbibition: A study on a correlated random tube network. *Geophysical Journal International*, *212*(2), 1398–1411. <https://doi.org/10.1093/gji/ggx474>
- Minagawa, H., Nishikawa, Y., Ikeda, I., Miyazaki, K., Takahara, N., Sakamoto, Y., et al. (2008). Characterization of sand sediment by pore size distribution and permeability using proton nuclear magnetic resonance measurement. *Journal of Geophysical Research*, *113*(B7), B07210. <https://doi.org/10.1029/2007JB005403>
- Ming, F., Li, D. Q., & Chen, L. (2020). Electrical resistivity of freezing clay: Experimental study and theoretical model. *Journal of Geophysical Research: Earth Surface*, *125*(2), e2019JF005267. <https://doi.org/10.1029/2019JF005267>
- Nishiyama, N., & Yokoyama, T. (2021). Water film thickness in unsaturated porous media: Effect of pore size, pore solution chemistry, and mineral type. *Water Resources Research*, *57*(6), e2020WR029257. <https://doi.org/10.1029/2020WR029257>
- Niu, F. J., Li, A. Y., Luo, J., Lin, Z. J., Yin, G. A., Liu, M. H., et al. (2017). Soil moisture, ground temperatures, and deformation of a high-speed railway embankment in Northeast China. *Cold Regions Science and Technology*, *133*, 7–14. <https://doi.org/10.1016/j.coldregions.2016.10.007>
- Oldenborger, G. A. (2021). Subzero temperature dependence of electrical conductivity for permafrost geophysics. *Cold Regions Science and Technology*, *182*, 103214. <https://doi.org/10.1016/j.coldregions.2020.103214>
- Oldenborger, G. A., & LeBlanc, A. M. (2018). Monitoring changes in unfrozen water content with electrical resistivity surveys in cold continuous permafrost. *Geophysical Journal International*, *72*(4), 177–187. <https://doi.org/10.1093/gji/ggy321>
- Oquist, M. G., Sparrman, T., Klemetsson, L., Drotz, S. H., Grip, H., Schleucher, J., & Nilsson, M. (2009). Water availability controls microbial temperature responses in frozen soil CO₂ production. *Global Change Biology*, *15*(11), 2715–2722. <https://doi.org/10.1111/j.1365-2486.2009.01898.x>
- Pedrazas, M. N., Cardenas, M. B., Demir, C., Watson, J. A., Connolly, C. T., & McClelland, J. W. (2020). Absence of ice-bonded permafrost beneath an Arctic lagoon revealed by electrical geophysics. *Science Advances*, *6*(43), eabb5083. <https://doi.org/10.1126/sciadv.abb5083>
- Pollock, D., & Cirkpa, O. A. (2012). Fully coupled hydrogeophysical inversion of a laboratory salt tracer experiment monitored by electrical resistivity tomography. *Water Resources Research*, *48*(1), W01505. <https://doi.org/10.1029/2011WR010779>
- Rembert, F., Jougnot, D., & Guarracino, L. (2020). A fractal model for the electrical conductivity of water-saturated porous media during mineral precipitation-dissolution processes. *Advances in Water Resources*, *145*, 103742. <https://doi.org/10.1016/j.advwatres.2020.103742>
- Revil, A. (2012). Spectral induced polarization of shaly sands: Influence of the electrical double layer. *Water Resources Research*, *48*(2), W02517. <https://doi.org/10.1029/2011WR011260>
- Revil, A., Coperey, A., Deng, Y., Cerepi, A., & Seleznev, N. (2018). Complex conductivity of tight sandstones. *Geophysics*, *83*(2), E55–E74. <https://doi.org/10.1190/geo2017-0096.1>
- Revil, A., Coperey, A., Shao, Z., Florsch, N., Fabricius, I. L., Deng, Y. P., et al. (2017). Complex conductivity of soils. *Water Resources Research*, *53*(8), 7121–7147. <https://doi.org/10.1002/2017WR020655>
- Revil, A., & Glover, P. W. J. (1997). Theory of ionic-surface electrical conduction in porous media. *Physical Review B*, *55*(3), 1757–1773. <https://doi.org/10.1103/PhysRevB.55.1757>
- Revil, A., Karaoulis, M., Johnson, T., & Kemna, A. (2012). Review: Some low-frequency electrical methods for subsurface characterization and monitoring in hydrogeology. *Hydrogeology Journal*, *20*(4), 617–658. <https://doi.org/10.1007/s10040-011-0819-x>
- Revil, A., Kessouri, P., & Verdín, C. T. (2014). Electrical conductivity, induced polarization, and permeability of the Fontainebleau sandstone. *Geophysics*, *79*(5), D301–D318. <https://doi.org/10.1190/geo2014-0036.1>
- Revil, A., Linde, N., Cerepi, A., Jougnot, D., Matthäi, S., & Finsterle, S. (2007). Electrokinetic coupling in unsaturated porous media. *Journal of Colloid and Interface Science*, *313*(1), 315–327. <https://doi.org/10.1016/j.jcis.2007.03.037>
- Revil, A., Soueid Ahmed, A., & Matthai, S. (2018). Transport of water and ions in partially water-saturated porous media: Part 3. Electrical conductivity. *Advances in Water Resources*, *121*, 97–111. <https://doi.org/10.1016/j.advwatres.2018.08.007>
- Shan, W., Liu, Y., Hu, Z. G., & Xiao, J. T. (2015). A model for the electrical resistivity of frozen soils and an experimental verification of the model. *Cold Regions Science and Technology*, *119*, 75–83. <https://doi.org/10.1016/j.coldregions.2015.07.010>
- Shen, Y., Wang, Y., Wei, X., Jia, H., & Yan, R. (2020). Investigation on meso-debonding process of the concrete interface induced by freeze-thaw cycles using NMR technology. *Construction and Building Materials*, *252*, 118962. <https://doi.org/10.1016/j.conbuildmat.2020.118962>
- Tai, B. W., Liu, J. K., & Chang, D. (2020). Experimental and numerical investigation on the sunny-shady slopes effect of three cooling embankments along an expressway in warm permafrost region, China. *Engineering Geology*, *269*, 105545. <https://doi.org/10.1016/j.enggeo.2020.105545>
- Tai, B. W., Liu, J. K., Yue, Z. R., Liu, J. Y., Tian, Y. H., & Wang, T. F. (2018). Effect of sunny-shady slopes and strike on thermal regime of subgrade along a high-speed railway in cold regions, China. *Engineering Geology*, *232*, 182–191. <https://doi.org/10.1016/j.enggeo.2017.09.002>
- Tang, L. Y., Wang, K., Jin, L., Yang, G. S., Jia, H. L., & Taoum, A. (2018). A resistivity model for testing unfrozen water content of frozen soil. *Cold Regions Science and Technology*, *153*, 55–63. <https://doi.org/10.1016/j.coldregions.2018.05.003>
- Teng, J. D., Kou, J. Y., Yan, X., Zhang, S., & Sheng, D. C. (2020). Parameterization of soil freezing characteristic curve for unsaturated soils. *Cold Regions Science and Technology*, *170*(68), 102928. <https://doi.org/10.1016/j.coldregions.2019.102928>
- Teng, J. D., Liu, J. L., Zhang, S., & Sheng, D. C. (2019). Modelling frost heave in unsaturated coarse-grained soils. *Acta Geotechnica*, *15*(11), 3307–3320. <https://doi.org/10.1007/s11440-020-00956-2>
- Teng, J. D., Liu, J. L., Zhang, S., & Sheng, D. C. (2022). Frost heave in coarse-grained soils: Experimental evidence and numerical modelling. *Géotechnique*, *73*, 1–12. <https://doi.org/10.1680/jgeot.21.00182>
- Thanh, L. D., Jougnot, D., Van Do, P., & Van Nghia, A. N. (2019). A physically based model for the electrical conductivity of water-saturated porous media. *Geophysical Journal International*, *219*(2), 866–876. <https://doi.org/10.1093/gji/ggz328>
- Thanh, L. D., Jougnot, D., Van Do, P., Tuyen, V. P., Ca, N. X., & Hien, N. T. (2020). A physically based model for the electrical conductivity of partially saturated porous media. *Geophysical Journal International*, *223*(2), 993–1006. <https://doi.org/10.1093/gji/ggaa307>
- Tokunaga, T. K. (2011). Physicochemical controls on adsorbed water film thickness in unsaturated geological media. *Water Resources Research*, *47*(8), W08514. <https://doi.org/10.1029/2011WR010676>
- Tyler, S. W., & Wheatcraft, S. W. (1990). Fractal processes in soil water retention. *Water Resources Research*, *26*(5), 1047–1054. <https://doi.org/10.1029/WR026i005p01047>

- Wang, C., Lai, Y., & Zhang, M. (2017). Estimating soil freezing characteristic curve based on pore-size distribution. *Applied Thermal Engineering*, 124, 1049–1060. <https://doi.org/10.1016/j.applthermaleng.2017.06.006>
- Wang, L. Y., Liu, J. K., Yu, X. B., Wang, T. F., & Feng, R. L. (2021). A simplified model for the phase composition curve of saline soils considering the second phase transition. *Water Resources Research*, 57(1), e2020WR028556. <https://doi.org/10.1029/2020WR028556>
- Watanabe, K., & Flury, M. (2008). Capillary bundle model of hydraulic conductivity for frozen soil. *Water Resources Research*, 44(12), W12402. <https://doi.org/10.1029/2008WR007012>
- Watanabe, K., & Mizoguchi, M. (2002). Amount of unfrozen water in frozen porous media saturated with solution. *Cold Regions Science and Technology*, 34(2), 103–110. [https://doi.org/10.1016/S0165-232X\(01\)00063-5](https://doi.org/10.1016/S0165-232X(01)00063-5)
- Watanabe, K., & Osada, Y. (2017). Simultaneous measurement of unfrozen water content and hydraulic conductivity of partially frozen soil near 0°C. *Cold Regions Science and Technology*, 142, 79–84. <https://doi.org/10.1016/j.coldregions.2017.08.002>
- Weerts, A. H., Bouten, W., & Verstraten, J. M. (1999). Simultaneous measurement of water retention and electrical conductivity in soils: Testing the Mualem-Friedman Tortuosity Model. *Water Resources Research*, 35(6), 1781–1787. <https://doi.org/10.1029/1999WR900022>
- Wen, Z., Ma, W., Feng, W., Deng, Y., Wang, D., Fan, Z., & Zhou, C. (2012). Experimental study on unfrozen water content and soil matric potential of Qinghai-Tibetan silty clay. *Environmental Earth Sciences*, 66(5), 1467–1476. <https://doi.org/10.1007/s12665-011-1386-0>
- Xiao, Z., Lai, Y. M., & Zhang, M. Y. (2018). Study on the freezing temperature of saline soil. *Acta Geotechnica*, 13(1), 195–205. <https://doi.org/10.1007/s11440-017-0537-1>
- Yu, B., & Cheng, P. (2002). A fractal permeability model for bi-dispersed porous media. *International Journal of Heat and Mass Transfer*, 45(14), 2983–2993. [https://doi.org/10.1016/S0017-9310\(02\)00014-5](https://doi.org/10.1016/S0017-9310(02)00014-5)
- Yu, B., Li, J., Li, Z., & Zou, M. (2003). Permeabilities of unsaturated fractal porous media. *International Journal of Multiphase Flow*, 29(10), 1625–1642. [https://doi.org/10.1016/S0301-9322\(03\)00140-X](https://doi.org/10.1016/S0301-9322(03)00140-X)
- Zhang, C., & Liu, Z. (2018). Freezing of water confined in porous materials: Role of adsorption and unfreezable threshold. *Acta Geotechnica*, 13(5), 1203–1213. <https://doi.org/10.1007/s11440-018-0637-6>
- Zhang, C., & Lu, N. (2018). What is the range of soil water density? Critical reviews with a unified model. *Reviews of Geophysics*, 56(3), 532–562. <https://doi.org/10.1029/2018RG000597>
- Zhang, Y. Z., Ma, W., Wang, T. L., Cheng, B. Y., & Wen, A. (2019). Characteristics of the liquid and vapor migration of coarse-grained soil in an open-system under constant-temperature freezing. *Cold Regions Science and Technology*, 165, 102793. <https://doi.org/10.1016/j.coldregions.2019.102793>
- Zhou, J., Meng, X., Wei, C., & Pei, W. (2020). Unified soil freezing characteristic for variably-saturated saline soils. *Water Resources Research*, 56(7), e2019WR026648. <https://doi.org/10.1029/2019WR026648>

References From the Supporting Information

- Heberling, F., Bosbach, D., Eckhardt, J. D., Fischer, U., Glowacki, J., Haist, M., et al. (2014). Reactivity of the calcite–water-interface, from molecular scale processes to geochemical engineering. *Applied Geochemistry*, 45, 158–190. <https://doi.org/10.1016/j.apgeochem.2014.03.006>
- Heberling, F., Trainor, T. P., Lützenkirchen, J., Eng, P., Denecke, M. A., & Bosbach, D. (2011). Structure and reactivity of the calcite–water interface. *Journal of Colloid and Interface Science*, 354(2), 843–857. <https://doi.org/10.1016/j.jcis.2010.10.047>
- Leroy, P., & Revil, A. (2004). A triple-layer model of the surface electrochemical properties of clay minerals. *Journal of Colloid and Interface Science*, 270(2), 371–380. <https://doi.org/10.1016/j.jcis.2003.08.007>
- Tang, R., Zhou, G. Q., Jiao, W., & Ji, Y. K. (2019). Theoretical model of hydraulic conductivity for frozen saline/non-saline soil based on freezing characteristic curve. *Cold Regions Science and Technology*, 165, 102794. <https://doi.org/10.1016/j.coldregions.2019.102794>
- Zimmermann, R., Dukhin, S., & Werner, C. (2001). Electrokinetic measurements reveal interfacial charge at polymer films caused by simple electrolyte ions. *The Journal of Physical Chemistry B*, 105(36), 8544–8549. <https://doi.org/10.1021/jp004051u>